

See discussions, stats, and author profiles for this publication at: <https://www.researchgate.net/publication/330116366>

Definition of Seismic Input From Fault-Based PSHA: Remarks After the 2016 Central Italy Earthquake Sequence

Article in *Tectonics* · January 2019

DOI: 10.1029/2018TC005086

CITATION

1

READS

193

6 authors, including:



Alessandro Valentini

Università degli Studi G. d'Annunzio Chieti e Pescara

12 PUBLICATIONS 37 CITATIONS

[SEE PROFILE](#)



B. Pace

Università degli Studi G. d'Annunzio Chieti e Pescara

76 PUBLICATIONS 826 CITATIONS

[SEE PROFILE](#)



Paolo Boncio

Università degli Studi G. d'Annunzio Chieti e Pescara

111 PUBLICATIONS 1,943 CITATIONS

[SEE PROFILE](#)



Francesco Visini

National Institute of Geophysics and Volcanology

59 PUBLICATIONS 358 CITATIONS

[SEE PROFILE](#)

Some of the authors of this publication are also working on these related projects:



URBISIT [View project](#)



Site effects [View project](#)

Tectonics

RESEARCH ARTICLE

10.1029/2018TC005086

Special Section:

The 2016 Central Italy Seismic Sequence: Insights, implications and lessons learned

Key Points:

- A fault-based and time-dependent approaches give a complementary view of PSHA
- We provide Input ground motion for site effects studies in central Italy
- We consider this approach useful for reconstruction projects

Supporting Information:

- Supporting Information S1
- Data Set S1
- Data Set S2

Correspondence to:

B. Pace,
bruno.pace@unich.it

Citation:

Valentini, A., Pace, B., Boncio, P., Visini, F., Pagliaroli, A., & Pergalani, F. (2019). Definition of seismic input from fault-based PSHA: Remarks after the 2016 central Italy earthquake sequence. *Tectonics*, 38. <https://doi.org/10.1029/2018TC005086>

Received 3 APR 2018


Accepted 28 DEC 2018

Accepted article online 3 JAN 2019

©2019. The Authors.

This is an open access article under the terms of the Creative Commons Attribution-NonCommercial-NoDerivs License, which permits use and distribution in any medium, provided the original work is properly cited, the use is non-commercial and no modifications or adaptations are made.

Definition of Seismic Input From Fault-Based PSHA: Remarks After the 2016 Central Italy Earthquake Sequence

A. Valentini^{1,2}, B. Pace¹ , P. Boncio¹, F. Visini³, A. Pagliaroli² , and F. Pergalani⁴

¹CRUST-DiSPUTer Department, Università degli Studi "G. d'Annunzio" di Chieti-Pescara, Chieti, Italy, ²InGeo Department, Università degli Studi "G. d'Annunzio" di Chieti-Pescara, Chieti, Italy, ³Istituto Nazionale di Geofisica e Vulcanologia - Sezione di Pisa, Pisa, Italy, ⁴Dipartimento di Ingegneria Civile e Ambientale, Politecnico di Milano, Milan, Italy

Abstract This work focuses on how the progress in earthquake science that follows a large, deeply studied earthquake might be promptly combined with updated approaches of seismic hazard analysis to guide applicative choices for seismic risk reduction, such as postevent seismic microzoning and building design. Both seismic microzoning and seismic design of structures require strong motion records to perform numerical site response analyses. These records have to be related to the seismotectonic context and historical seismicity of the investigation area. We first performed a fault-based probabilistic seismic hazard analysis in the area struck by the 2016 central Italy seismic sequence to individuate reference uniform hazard spectra at rock conditions. We used two different seismic hazard models, one considering 27 individual seismogenic sources (ISSs), and the second one involving grid point seismicity, using a fixed-radius smoothing approach. The geological and seismotectonic data of the 2016 seismic sequence were used to update the model of ISSs. We performed a deaggregation analysis to evaluate the contribution of the ISS in the hazard of four representative sites and to select the magnitude-distance pairs useful in the selection of the real accelerograms. The deaggregation analysis has been performed to identify which source and magnitude most contribute to the hazard for each site, and for different periods of spectral accelerations. Finally, we select, for each site, a set of natural accelerograms, from both nonimpulsive and pulse-like records, based on the magnitude-distance pairs that are compatible on average with target uniform hazard spectra.

1. Introduction

When a large earthquake strikes a developed area, several fields, seismological, geodetic, and theoretical studies follow the event, producing important progress in earthquake science at both local and wider scales. Urgent actions aimed at quantifying the local seismic hazard for postevent reconstruction might largely benefit from this improved knowledge, starting from an updated assessment of the expected ground shaking, but it is not always possible due to both temporal and methodological reasons. For these reasons it is important to develop and strengthen modern seismic hazard studies that can give in a short time new evaluation of the expected ground motion, taking into account all the progresses, useful for reconstruction projects.

In the last 10 years, central Italy has been struck several times by moderate to strong earthquakes, with a moment magnitude (M_w) up to 6.5. The mainshocks of last two seismic sequences, that is, L'Aquila 2009 and central Italy 2016, have destroyed or partially destroyed several municipalities, such as L'Aquila, Poggio Picenze, Amatrice, Pescara sul Tronto, Accumoli, and Camerino. In addition to economic losses due to the collapsed or damaged buildings such as schools, hospitals, churches, and houses, these events also caused several fatalities (more than 600 in the last 10 years).

Fatalities and economic loss can be reduced by tools operating at the building scale (i.e., up-to-date building codes and seismic retrofiting programs) and at the urban scale (i.e., seismic microzoning, SM) to be included in urban/territory planning tools. Both tools for seismic risk mitigation, namely building code and SM, operate therefore at different scales; however, they share some aspects such as the assessment of local seismic hazard or site effects (Pagliaroli, 2018). It should be pointed out that the quantitative assessment of site effects, even with a lower accuracy with respect to a site response study at building scale, is required by the highest levels of SM (i.e., level-3 SM; SM Working Group, 2015; TC4-ISSMGE, 1993, revised 1999), while at basic level of SM (level-1) the site effects are defined qualitatively based on geological and morphological

features. The quantitative evaluation of site effects, for both seismic design and level-3 SM studies, is usually achieved by means of numerical site response analyses carried out with 1D or 2D computer codes requiring acceleration time histories as input motion at the outcropping seismic bedrock. According to current European (Eurocode 8 Part 1, European Standard EN 1998–1, 2004) and Italian (i.e., Norme Tecniche per le Costruzioni (NTC), 2018) building codes, for geotechnical applications, these accelerograms must be real recordings, while artificial or hybrid signals are not allowed, and they are selected to be compatible with a reference or target spectrum at rock site conditions. In literature, there are several different methods for the selection of sets of real recordings based on different criteria (Haselton et al., 2009). The most common methods used as target spectrum are the uniform hazard spectrum (UHS) or the conditional mean spectrum. The UHS is determined by performing a Probabilistic Seismic Hazard Analysis (PSHA) in order to define the spectral acceleration (SA) for each period. Moreover, it has been used for the selection of real recordings over the past 20 years and it is implemented in several building codes (e.g., NTC, 2018, Eurocode 8). The conditional mean spectrum is a spectrum that matches the UHS at a conditioning period and represents also the response from a single earthquake scenario (Baker, 2011; Carlton & Abrahamson, 2014; Lin et al., 2013). For the purposes of this work, we used the UHS derived from PSHA, which reflects the seismotectonic context and historical seismicity of the investigated region.

We performed a fault-based PSHA of the area struck by the 2016 seismic sequence to obtain the reference response spectra at rock conditions at four representative sites: Perugia, Norcia, L'Aquila, and Sulmona. The use of active faults is becoming a consolidated approach in regions with moderate-to-low strain rates, such as France (Scotti et al., 2014), SE Spain (García-Mayordomo et al., 2007) and Italy (Peruzza et al., 2011; Valentini et al., 2017). In Valentini et al. (2017) the authors performed a fault-based PSHA for the whole of Italy, using two models of seismicity, distributed and fault source, integrated into a single model. Following this approach, we first updated the model of seismogenic sources by considering the seismotectonics of the 2016 earthquakes and then focusing only in the central part of Italy; we defined 27 Individual Seismogenic Sources (ISSs) for PSHA. Having completed the PSHA analysis, we computed the UHS and used it as target spectra in the choice of the strong motion records for the four investigation sites. Then, we performed a deaggregation analysis to individuate the ISSs that mainly contribute to the hazard of the investigation sites and to select the magnitude-distance (M-R) pair for the choice of the real accelerograms (e.g., Pace et al., 2008). Moreover, additional deaggregation analysis was performed for (i) different SAs in order to address the questions of whether the seismic hazard of a given source depends on the different SA, and (ii) for different bin of magnitude in order to see what is the impact of the magnitude-frequency distribution (MFD) used to compute the occurrence rates of a given source in the selection of the M-R pairs.

2. Seismotectonic Model

2.1. Seismotectonic Framework

The 2016 earthquake sequence occurred within the Apennines of central Italy (Figures 1 and 2), an area presently affected by NE directed extension at rates of 2–3 mm/yr, according to Global Positioning System data (Carafa & Bird, 2016; Cheloni et al., 2017; D'Agostino, 2014; D'Agostino et al., 2009; Devoti et al., 2011). The extension is accommodated by systems of NW-SE striking normal faults, dipping mostly to the SW (e.g., Boncio et al., 2004a; Brozzetti et al., 2009). The normal faults postdate the Apennine fold-and-thrust belt, a system of compressional structures formed by Mesozoic and Cenozoic carbonate and silicoclastic successions deformed during the Neogene Apennine orogeny (Barchi, 2010). Active normal faults are often the boundary of intermontane hanging wall basins filled by Pliocene-Quaternary sediments, on top of which small-to-intermediate size towns are located, such as L'Aquila (69,000 inhabitants) or Norcia (5,000 inhabitants) towns, affected by the 2009 and 2016 earthquakes. The present activity of the Apennine normal faults is constrained by several evidences, including Late Pleistocene-Holocene slip from fault scarp analysis (Galadini & Galli, 2000; Roberts & Michetti, 2004; Schlagenhauf et al., 2011), paleoearthquakes (Cinti et al., 2011; Galli et al., 2008, 2015), historical earthquakes (Galli, Castenetto, & Peronace, 2017; Rovida et al., 2016), and instrumental seismicity (Chiaraluca et al., 2017; De Nardis et al., 2011; Lavecchia et al., 2012). The active normal faults range in length mostly between 15 and 30 km. The slip rates, mostly derived from paleoseismological data or from profiles of Late Quaternary fault scarps (post-15 ± 3 kyrs ago), range from 0.2–0.5 to 1.4 mm/year, with such a large variability often due to chronologic uncertainties (see compilation in Pace et al., 2006, 2011, 2014, and references therein).

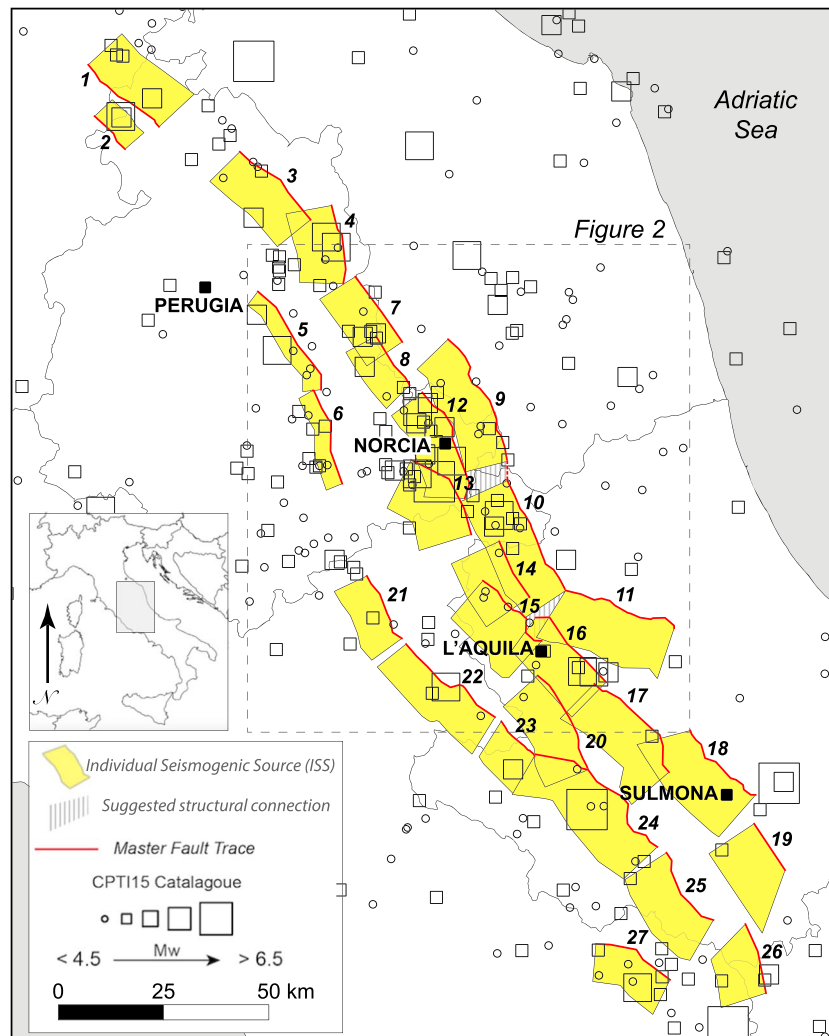


Figure 1. ISSs used in this work with their surface trace (red line) and their fault plane projection (yellow box); by empty and full squares, respectively, the epicenters of the events in CPTI15 catalog (Rovida et al., 2016) and the four sites where the deaggregation analysis has been performed. The numbers represent the identification number of each ISS (see Tables 1–3 for details). Dashed rectangle is the area represented in Figure 2. ISSs = individual seismogenic sources.

The 2016 earthquakes reactivated the Mount Vettore-Mount Bove and Mount Gorzano faults, belonging to the easternmost system of the Apennine normal faults. Both faults were considered active on the basis of geological evidence of Late Pleistocene-Holocene faulting, with slip rates estimated to be of ~1 and 0.7–0.9 mm/year for the Mount Vettore-Mount Bove and Mount Gorzano faults, respectively (Blumetti et al., 1993; Boncio et al., 2004b; Calamita & Pizzi, 1992; Galadini & Galli, 2000). Galadini and Galli (2003) carried out paleoseismological investigations on a synthetic splay of the Mount Vettore-Mount Bove fault and found evidence of at least two paleoearthquakes during the second half of the Holocene, with an elapsed time since the most recent event (pre-2016) of >1,500 years. To our knowledge, there are no historical earthquakes that can be associated with this fault. On the Mount Gorzano fault, Galadini and Galli (2003) found two paleoearthquakes younger than 8,300 years Before Present. According to Boncio et al. (2004b), the northern half of the fault was activated by the M_w 6.2 1639 earthquake. Part of the southern half of the faults was also activated by a strong aftershock (M_w 5.2) of the 2009 L'Aquila earthquake (M_w 6.3, Lavecchia et al., 2012).

The 24 August 2016, earthquake (M_w 6.0) nucleated in the stepover zone between the Mount Vettore-Mount Bove and Mount Gorzano faults and ruptured the southern portion of the Mount Vettore-Mount Bove fault up to the surface. Simultaneously, the same event ruptured the northern portion of the Mount Gorzano fault in the subsurface, with subtle evidence of surface faulting, limited to a very short portion

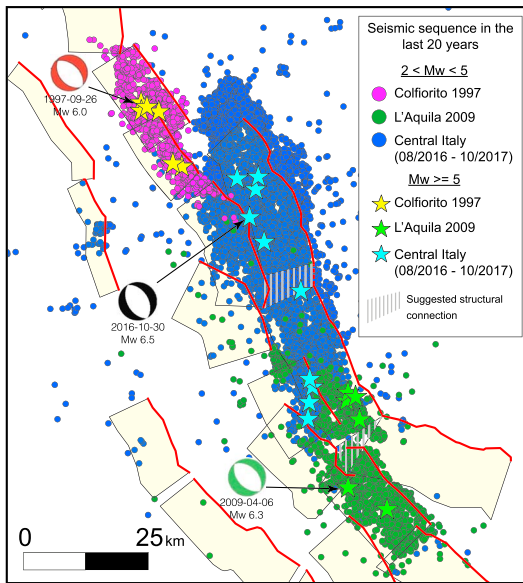


Figure 2. Instrumental seismicity in the last 20 years in the central Apennine. The magenta, green, and blue dots are all the earthquakes with a magnitude between 2 and 5, and occurred during the Colfiorito 1997, L'Aquila 2009, and Central Italy 2016 seismic sequences, respectively. Instead, the yellow, light green, and cyan stars are all the earthquakes with a magnitude higher or equal than 5. The mainshocks of each sequence have been reported the focal mechanisms. The epicenters and the focal mechanism for each sequence come from Chiaraluca et al. (2004, 2011, 2017), for Colfiorito, L'Aquila, and Central Italy, respectively. The central Italy seismic sequence has been updated with the epicenters from ISIDE (<http://iside.rm.ingv.it>) occurred after Chiaraluca et al., 2017. See Figure 1 for the location of the area. ISIDE = Italian seismological instrumental and parametric database.

destroyed by the 2016 seismic sequence. The model consists of 27 ISSs lying within a distance of ~100 km from the 30 October mainshock. The contribution of more distant sources can be considered negligible. The ISS model derives from Boncio et al. (2004a), implemented with data from Brozzetti et al. (2009) for the area north of Perugia and from Pace et al. (2011) for the area around L'Aquila. The ISSs correspond to faults with a simplified geometry, dipping on average 50° to the SW except for the faults north of Perugia (1 and 2 in Figure 1), which dip to the NE at 30–40°. The bottom of the seismogenic layer ranges from ~6 km in the northwestern sector (south of Perugia) to 14–15 km in the southern-eastern sector of the study area (Boncio et al., 2004a). Seismogenic depths of the ISSs are given in Table 2.

The geometry of the Mount Vettore-Mount Bove and Mount Gorzano faults was updated, thanks to the seismotectonics of the 2016 earthquakes (Brozzetti et al., 2019; Chiaraluca et al., 2017; Civico et al., 2018; Lavecchia et al., 2016; Pouse et al., 2018 Figure 2). The fault lengths are now constrained at 34 and 30 km for the Mount Vettore-Mount Bove and Mount Gorzano faults, respectively. By approximating the faults to a planar surface with a constant dip, which we consider an appropriate simplification for the purposes of our modeling, the average dip angle, constrained by earthquake focal mechanisms, is 47° for the Mount Vettore-Mount Bove fault (30 October 2016 TDMT solution; <http://cnt.rm.ingv.it/en/tdmt>) and 45° for the Mount Gorzano fault (average of the last six TDMT solutions of earthquakes with $M_w \geq 5$; 29 April 2009; 24 August 2016; four events of 18 January 2017). The thickness of the seismogenic layer is constrained at 11 and 12 km for Mount Vettore-Mount Bove and Mount Gorzano faults, respectively, thanks to the depth distribution of aftershocks (Chiaraluca et al., 2017; Valoroso et al., 2013). The rake of the average slip vector of the ISSs was calculated by projecting onto the fault surface the minimum regional deviatoric stress (Boncio et al., 2004a; Brozzetti et al., 2009) or the direction of the GPS-determined maximum horizontal extension (D'Agostino, 2014); instead, the slip vector of the Mt. Vettore - Mt. Bove fault was derived from the 30 October 2016 TDMT solution.

of the fault (Lavecchia et al., 2016; Pucci et al., 2017). Two earthquakes on 26 October 2016 (M_w 5.4, M_w 5.9) ruptured up to the surface of the northern portion of the Mount Vettore-Mount Bove fault. Then, the 30 October event (M_w 6.5) ruptured almost entirely the Mount Vettore-Mount Bove fault, reactivating also the 24 August and 26 October fault sections (Civico et al., 2018; Villani et al., 2018). The end-to-end length of the surface rupture is ~30 km, which is close to the entire length of the geologic fault (~34 km, this work). On 18 January 2017, four moderate earthquakes (M_w 5.1, 5.5, 5.4 and 5.0) ruptured the Mount Gorzano fault south of the 24 August shock (Chiaraluca et al., 2017).

The cumulated moment released by the ruptures ($M_w > 5.0$) on the Mount Vettore-Mount Bove fault from 24 August to 30 October is equivalent to the moment release of a single M_w 6.6–6.7. Therefore, the 2016 sequence released almost entirely the maximum magnitude expected in the literature on the fault (from 6.5 to 6.7–6.9; Galadini & Galli, 2003; Pace et al., 2006). On the contrary, we estimate that the cumulated moment released the Mount Gorzano fault (April 2009, 24 August 2016, and 18 January 2017), corresponding to a cumulated M_w of ~6.1, is still far from the maximum magnitude expected in the literature on the fault (6.6–6.7; Galadini & Galli, 2003; Pace et al., 2006). Verdecchia et al. (2018) recently suggested a contribution of the coseismic and postseismic viscoelastic stress transfer in controlling the seismic sequence evolution, including the participation of the two major faults.

2.2. Individual Seismogenic Sources

In our seismic hazard model, an ISS is an individual structure liable to generate major earthquakes ($M \geq 5.5$), for which the measured maximum rupture length and maximum rupture area can be used to infer the maximum expected magnitude and slip per event. Figure 1 illustrates the ISS model used in this study for analyzing the seismic hazard in the area

The associations of the ISSs to historical or paleoearthquakes, recently revised by Valentini et al. (2017) using the most recent earthquake catalog (CPTI 15, Rovida et al., 2016) and the most updated paleoseismological literature, are summarized in Table 1. The geometric (length, dip, and thickness of the seismogenic layer) and kinematic (rake, slip rate) parameters of the ISSs are listed in Table 2. Concerning the geological slip rates, in Table 2 we list the minimum and maximum values compiled in Valentini et al. (2017) and determined by several authors in different ways over different time scales (e.g., from 10^3 to 10^5 years; references in Valentini et al., 2017). An aseismic factor was not taken into account because we assumed that slip rate is representative of only seismic slip; this assumption could be an issue explored in a future work. According to consolidated practice, geometrical parameters of an ISS and its slip rate can be used to calculate the global budget of the seismic moment rate allowed by a source. Basing on the tool developed in Pace et al. (2016), *FiSH-Fault data Into Seismic Hazard*, we derived the maximum earthquake and its uncertainty by empirical regression on length, area and magnitude, and recurrence intervals of the maximum magnitude from the slip rate. Details on these calculations, from the needed assumption to the evaluated seismic rates of occurrence, are described in section 3.1.

3. Seismic Hazard Analyses

One of the aims of this work is the definition of UHS to use as target spectra in the selection of (seven) real recorded accelerograms, useful to perform site-specific ground response analysis, to carry out nonlinear dynamic analysis of a building or structure sitting on outcropping bedrock, and to model the expected ground motion in high-level SM studies. According to the Italian National Building Code (NTC, 2018), the accelerograms have to be compatible with the elastic response spectra at the site. Therefore, the choice of the recorded accelerograms has to be related to a good knowledge of the seismotectonic context and seismic hazard of the site, which controls the magnitude, distance, and kinematics of the seismogenic sources that mostly contribute to the hazard. In order to select the appropriate UHS for each investigation site, we performed a PSHA based on the integration of faults and past earthquakes. In particular, two earthquake-source models are considered in this work: the first involves active faults, and geological slip rates were used to quantify the seismic activity rate over a certain range of magnitude; the second involves grid point seismicity, with a fixed-radius smoothing approach, in which a historical catalog was used to evaluate seismic activity rates of expected earthquakes with a minimum M_w of 4.5 but excludes earthquakes associated with known faults (modified earthquake catalog). Because our final seismic hazard model requires the combination of the two source models, these were treated as complementary and not independent models, in terms of both the magnitude and frequency distribution, and together account for the spatial and temporal distribution of the seismicity in the study area. In the following subsections, we describe the two source models and how they are combined in the final seismic hazard model.

3.1. ISS Input

The ISSs used in this PSH model have been described in the previous section. However, in the use of active faults for PSHA, other important aspects need to be considered: maximum expected magnitude (M_{\max}), the seismogenic potential (e.g., seismic moment rate), and the selection of an appropriate MFD to characterize the temporal model describing the seismic activity of faults.

In this work, we evaluated the MFD using two models: a *Characteristic Gaussian Brownian Passage Time* (CHBPT) model centered at the maximum magnitude, as given by the following equation (Matthews et al., 2002)

$$P(t) = \sqrt{\frac{T_{\text{mean}}}{2\pi CV^2 T_e^3}} e^{\frac{(T_e - T_{\text{mean}})^2}{2T_{\text{mean}} CV^2 T_e}} \quad (1)$$

where the probability of occurrence $P(t)$ is the function of the elapsed time from the last earthquake (T_e) following a renewal process, and a *Truncated Gutenberg-Richter* (TGR) model (Kagan, 2002), as

$$\lambda(M) = \lambda_0 \frac{\exp(-\beta M) - \exp(-\beta M_u)}{\exp(-\beta M_0) - \exp(-\beta M_u)} \quad (2)$$

where the magnitude (M) is in the range of M_0 (minimum magnitude) to M_u (upper or maximum

Table 1
Earthquake Source Association Adopted for the Individual Seismogenic Source Input

n.	ISS name	Historical (post-1000 CE)				Instrumental		Paleoseismological	
		dd/mm/yyyy	I_0	M_w	sD	dd/mm/yyyy	M_w	Age ^a	Ref ^b
1	Città di Castello	18/10/1389	IX	6.0	0.5				
		26/04/1458	VIII–IX	5.8	0.5				
		30/09/1789	IX	5.9	0.1				
2	M. S. Tiberina	25/12/1352	IX	6.3	0.2				
		26/04/1917	IX–X	6.0	0.1				
3	Gubbio					29/04/1984	5.6		
4	Gualdo Tadino	17/04/1747	IX	6.1	0.1				
		27/07/1751	X	6.4	0.1				
5	Umbra Valley N	13/01/1832	X	6.4	0.1				
		12/02/1854	VIII	5.6	0.3				
6	Umbra Valley S	05/06/1767	VII–VIII	5.5	0.4				
		15/09/1878	VIII	5.5	0.2				
7	Colfiorito	30/04/1279	IX	6.2	0.2	26/09/1997	6.0		
8	Cesi - Civitella	11/10/1791	VIII	5.6	0.2	14/10/1997	5.6		
		14/02/1838	VIII	5.5	0.4				
9	Mount Vettore – Mount Bove					30/10/2106	6.5	+250/+450 –2200/–1800 –3700/–2800 –6000/–4000	12
10	Mount Gorzano	07/10/1639	XI–X	6.2	0.2			8320/+1000	1
		28/04/1646	IX	5.9	0.4			8425/8365	
11	Gran Sasso							3381/+1000	1
								6573/5475 16000/13000	
12	Nottoria-Preci	01/12/1328	X	6.5	0.3	19/09/1979	5.8	+1400/+1800	1
		14/01/1703	XI					–500/–50	
		27/06/1719	VIII	6.9	0.1				
		12/05/1730	IX						
		22/08/1859	VIII–IX	5.6	0.3				
		23/02/1879	VIII	6.0	0.1				
13	Cascia Cittareale			5.7	0.3				
				5.6	0.3				
14	Monte Reale	06/11/1599	IX	6.1	0.2				
		16/11/1916	VIII	5.5	0.1				
15	Pizzoli Pettino	02/02/1703	X	6.7	0.1			+1400/+1800	1
16	Paganica	27/11/1461	X	6.5	0.5	06/04/2009	6.3	+890/+1150	2,3,4
								–760/+670	5
17	Middle Aternum Valley							–2900/–760	
18	Sulmona							II–I sec. BCE	6
								6381/3511	
								+80/+240 (II s.) ~ 4500 8450/6315 after 9000	7
19	Pizzalto C.Miglia							–800/+1030	1,8
								5685/4890	
20	Campo Felice Ovindoli							+890/XIII sec.	1,9
								3830/3375 7560–4980	
21	Rieti	01/12/1298	IX–X	6.3	0.5				
22	Salto Valley	09/09/1349	IX	6.3	0.1				
23	Velino	24/02/1904	IX	5.7	0.1			1400–1000 BP	10
24	Fucino	13/01/1915	XI	7	0.1			+426/+782	1,10
								3500–3300	11
								5944–5618	

Table 1 (continued)

n.	ISS name	Historical (post-1000 CE)				Instrumental		Paleoseismological	
		dd/mm/yyyy	I_0	M_w	sD	dd/mm/yyyy	M_w	Age ^a	Ref ^b
25	Marsicano								
26	Barrea					07/05/1984	5.9		
27	Sora	24/07/1654	XI-X	6.3	0.1				

Note. I_0 , epicentral intensity; M_w , moment magnitude, and its standard deviation (sD). ISS = individual seismogenic source; CE = Common Era; BCE = Before Common Era.

^aIf the age of paleoearthquake is preceded by a + or -, we refer to the CE and BCE, respectively, otherwise we refer to BP age (Before Present, starting from 1950). ^bRef = Reference: 1, Galli et al. (2008); 2, Cinti et al. (2011); 3, Galli et al. (2010); 4, Galli et al. (2011); 5, Moro et al. (2013); 6, Falcucci et al. (2011); 7, Galli et al. (2015); 8, D'Addezio et al. (2001); 9, Salvi et al. (2003); 10, Schlagenhauf et al. (2011); 11, Galli et al. (2012); 12, Galli, Galderisi, et al. (2017).

magnitude); otherwise, $\lambda(M)$ is 0. Additionally, λ_0 is the smoothed rate of earthquakes at $M_w = 5.5$ and $\beta = b \ln(10)$.

Because the choice of the *appropriate* MFD for each individual source depends on the knowledge of the fault and data availability, this could be a difficult task. Based on the fault database in Tables 1 and 2 and in order to choose the appropriate MFD, we explored several aspects associated with defining an ISS input—maximum magnitude (M_{\max}); mean recurrence time (T_{mean}) and its coefficient of variation (CoV) defined as the ratio between the standard deviation of T_{mean} and T_{mean} ; and time elapsed (T_e) from the last event—and then we computed the expected seismicity rate.

Table 2
Geometric Parameters of the Individual Seismogenic Sources

n.	ISS name	L (km)	Dip (deg)	Seismogenic thickness (km)	Rake (deg)	SR _{min} (mm/year)	SR _{max} (mm/year)
1	Città di Castello	22.7	30	7	-93	0.35	1.1
2	M. S. Tiberina	10.8	30	3.5	-93	0.35	1.1
3	Gubbio	23.7	30	6	-86	0.4	1.2
4	Gualdo Tadino	19.3	35	8	-59	0.25	0.75
5	Umbra Valley N	28.6	50	4.5	-83	0.4	1.2
6	Umbra Valley S	24	50	4.5	-73	0.4	1.2
7	Colfiorito	19	37	8.5	-87	0.25	0.75
8	Cesi-Civitella	14	40	6.5	-87	0.3	0.9
9	Mount Vettore-Mount Bove	34	47	11	-89	0.35	1.05
10	Mount Gorzano	30	45	12	-84	0.7	1.1
11	Gran Sasso	28.7	50	15	-94	0.6	1
12	Nottoria-Preci	29	50	12	-81	0.7	0.9
13	Cascia-Cittareale	24.2	50	13.5	-86	0.3	0.9
14	Montereale	15.5	50	14	-94	0.3	0.9
15	Pizzoli-Pettino	21.5	50	14	-95	0.3	0.9
16	Paganica	20	50	14	-88	0.45	0.71
17	Middle Aternum Valley	29	50	14	-80	0.3	0.4
18	Sulmona	23.5	50	15	-90	0.5	0.7
19	Pizzalto-Cinque Miglia	18	50	15	-80	0.2	0.5
20	Campo Felice-Ovindoli	26.5	50	13	-84	0.7	1.2
21	Rieti	17.5	50	10	-80	0.3	0.5
22	Salto Valley	28.4	50	11	-92	0.5	0.7
23	Velino	11.5	50	12.5	-94	0.7	0.9
24	Fucino	38	50	13	-86	0.4	1.4
25	Marsicano	21	50	13	-86	0.5	0.7
26	Barrea	17.4	50	13	-66	0.2	0.6
27	Sora	20	50	11	-96	0.15	0.45

Note. L, along strike length; Dip, the inclination angle of the fault plane; Rake; the angle at which the hanging wall moves against the footwall in a fault; SR_{min} and SR_{max}, the minimum and maximum slip rate assigned to the ISSs. ISSs = individual seismogenic sources.

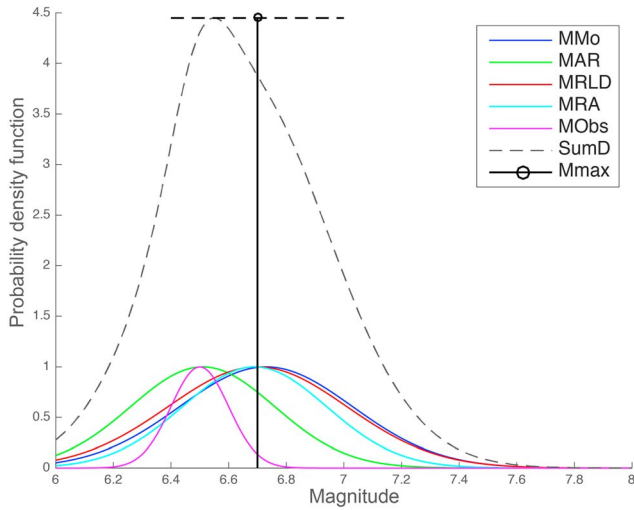


Figure 3. Example of the *MB FiSH* code (Pace et al., 2016) output for the Mount Vettore-Mount Bove fault. In this example, five magnitudes are estimated: M_{Mo} (blue line), based on the calculated scalar seismic moment; M_{AR} (green line), corresponding to the estimate based on aspect ratio (Peruzza et al., 2002); M_{RLD} (red line) and M_{RA} (cyan line), corresponding to estimates based on the maximum subsurface fault length and M_{RA} form the empirical relationships of Wells and Coppersmith (1994); and M_{Obs} (magenta line), corresponding to the largest observed moment magnitude (see Table 1 for details). The dashed black line (SumD) is the sum of each probability density function. The central value of this fit (vertical black line) represents the M_{max} value, and the horizontal dashed black line represents its standard deviation. M_{RA} = maximum rupture area; M_{RLD} = maximum subsurface rupture length; M_{AR} = M from aspect ratio.

3.1.1. The ISSs Seismogenic Potential: Maximum Magnitudes, Mean Recurrence Times, and CoVs

According to Pace et al. (2016), the geometric and slip rate data of an ISS can be used to estimate its seismogenic potential. To evaluate M_{max} of each source, we first computed and then combined up to four M_{max} estimates (see the example for Mount Vettore-Mount Bove source in Figure 3). Two of these four M_{max} were obtained by using the Wells and Coppersmith (1994) empirical relationships for the maximum rupture area (and maximum subsurface rupture length); a third M_{max} (M from aspect ratio) was computed by reducing the fault length input if the aspect ratio (W/L) is smaller than the value evaluated by the relation between the aspect ratio and rupture length derived by Peruzza and Pace (2002); and a fourth M_{max} (M_{Mo}) is based on the calculated scalar seismic moment (M_0) and the application of the standard formula $M_w = 2/3 (\log M_0 - 9.1)$, Hanks & Kanamori, 1979; International Association of Seismology and Physics of the Earth's Interior, 2005). Note that in this case, we used an assumed strain drop equal to 3×10^{-5} . As each of these four M_{max} is affected by an uncertainty of its estimation, following the approach of Pace et al. (2016), we created a probability curve for each magnitude, under the assumption that the uncertainty can be described by a normal distribution (Figure 3). Subsequently, we summed the probability density curves and fitted the summed curve to a normal distribution to obtain a mean of the four M_{max} and a standard deviation. Thus, a unique M_{max} with a standard deviation is computed for each source, and this value represents the maximum rupture that is allowed by the fault geometry and the rheological properties. We then compared the M_{max} with the maximum magnitude observed on the ISS from instrumental or historical catalog (M_{Obs}). Depending on the M_{Obs} values and its standard deviation in

respect to the computed M_{max} , we followed a different approach: (a) If $M_{Obs} + 1$ standard deviation was lower than $M_{max} - 1$ standard deviation, we kept M_{max} ; (b) if $M_{Obs} - 1$ standard deviation was larger than $M_{max} + 1$ standard deviation, we reviewed the fault geometry and/or the earthquake-source association; (c) if $M_{Obs} + 1$ standard deviation was within the range $M_{max} + 1$ standard deviation, we recomputed M_{max} by introducing a fifth probability density function given by M_{Obs} . In some way, we were using the observation to *update* or refining the empirical relationship. For this reason, and only in the case (c), we decided to use the M_{Obs} as an input for the mean and standard deviation calculation.

To obtain the T_{mean} of M_{max} , we used the criterion of *segment seismic moment conservation* proposed by Field et al. (1999). This criterion divides the seismic moment that corresponds to M_{max} by the moment rate given a slip rate:

$$T_{mean} = \frac{1}{Char\ Rate} = \frac{10^{(1.5M_{max}+9.1)}}{\mu VLW} \quad (3)$$

where T_{mean} is the mean recurrence time in years, *Char Rate* is the annual mean rate of occurrence, M_{max} is the computed mean maximum magnitude, μ is the shear modulus, V is the average long-term slip rate, and L and W are along-strike rupture length and downdip width, respectively. In addition to M_{max} and T_{mean} , we computed also the CoV, which in BPT function represents the uncertainty in the temporal behavior (Visini & Pace, 2014), defined as the ratio between the standard deviation of the recurrence times and T_{mean} computed by equation (3). The standard deviation of T_{mean} was computed taking into account the uncertainties in slip rate (Pace et al., 2016; Peruzza et al., 2010).

3.1.2. Elapsed Time Since the Last Event

Another critical parameter in time-dependent PSHA models is the time elapsed since the last maximum sized event (T_e ; Table 3). In this work we deduced T_e in three different cases: (i) when the last event is known; (ii) when the last event is a paleoseismological record (that is a range of occurrences); and (iii)

Table 3
List of M_{max} , sD of M_{max} , T_{mean} , CoV, and T_e Since the 2017 Obtained With MB FiSH Code (Pace et al., 2016) Using the Geometric Parameters Listed in Table 2 for Each ISS

n.	ISS name	M_{max}	sD	T_{mean}	CoV	M_{Obs}	sD	T_e	MFD
1	Città di Castello	6.3	0.4	566	1.47	6.0	0.5	228	CHBPT
2	M. S. Tiberina	6.0	0.3	766	1.16	6.3	0.2	100	CHBPT
3	Gubbio	6.4	0.2	962	0.85	-	-	33	TGR
4	Gualdo Tadino	6.4	0.2	1241	0.85	6.4	0.1	266	CHBPT
5	Umbra Valley N	6.3	0.4	2411	1.47	6.4	0.1	185	TGR
6	Umbra Valley S	6.2	0.4	1707	1.47	-	-	139	TGR
7	Colfiorito	6.4	0.2	1245	0.85	6.2	0.2	20	TGR
8	Cesi-Civitella	6.1	0.3	698	1.15	-	-	20	TGR
9	Mount Vettore-Mount Bove	6.7	0.3	2042	1.15	6.5	0.1	1	CHBPT
10	Mount Gorzano	6.6	0.2	898	0.73	-	-	378	TGR
11	Gran Sasso	6.7	0.3	1090	1.07	-	-	3417	CHBPT
12	Nottoria-Preci	6.6	0.2	1173	0.70	6.9	0.1	314	TGR
13	Cascia-Cittareale	6.5	0.2	922	0.85	-	-	418	TGR
14	Montereale	6.3	0.3	696	1.15	-	-	^a	CHBPT
15	Pizzoli-Pettino	6.5	0.2	1001	0.85	6.7	0.1	314	CHBPT
16	Paganica	6.5	0.2	1113	0.73	6.5	0.5	8	CHBPT
17	Middle Aternum Valley	6.6	0.2	2009	0.71	-	-	2217	CHBPT
18	Sulmona	6.5	0.2	855	0.71	-	-	1917	CHBPT
19	Pizzalto-Cinque Miglia	6.4	0.3	1354	1.12	-	-	987	CHBPT
20	Campo Felice-Ovindoli	6.6	0.2	851	0.74	-	-	702	CHBPT
21	Rieti	6.3	0.3	1294	1.07	6.3	0.5	719	CHBPT
22	Salto Valley	6.5	0.2	1302	0.71	-	-	668	CHBPT
23	Velino	6.1	0.3	395	1.04	-	-	113	CHBPT
24	Fucino	6.8	0.3	1791	1.18	7.1	0.1	102	CHBPT
25	Marsicano	6.5	0.2	1104	0.71	-	-	^a	CHBPT
26	Barrea	6.3	0.3	1001	1.15	-	-	33	TGR
27	Sora	6.4	0.2	1939	0.85	6.3	0.1	363	CHBPT

Note. M_{Obs} is the maximum observed magnitude (see text for more details) with its standard deviation (sD). The last column is the MFD model (between CHBPT and TGR) selected. MFD = magnitude-frequency distribution; TGR = Truncated Gutenberg-Richter; CHBPT = CHaracteristic Gaussian Brownian Passage Time; CoV = coefficient of variation; BPT = Brownian Passage Time.

^aFor Montereale and Marsicano sources, instead of computing the T_e , we computed the BPT/Poisson ratio and then multiplied the Poisson probability in order to obtain a renewal time-dependent probability of occurrence for the next 50 years (see text for more details). The ratios are equal to 0.7 and 1.3, for Montereale and Marsicano, respectively.

when no information about historical and paleo earthquakes is available. For the first case, the simplest one, we assigned the T_e starting from 2017, as for example the Paganica fault (last event age 2009, $T_e = 8$ years) and Fucino fault (last event age 1915, $T_e = 102$ years). In the second case, when only paleoseismological constraints are available, we picked up the lowest boundary of the last event (longest T_e). In some cases, when it is suggested from the authors of the paleoseismological investigations, we picked up the upper boundary of the last event such as, for example, for the Pizzalto-Cinque Miglia (D'Addezio et al., 2001) and Campo Felice-Ovindoli (Salvi et al., 2003, and reference therein) faults. Data used to derive T_e were analyzed from the available literature (e.g., Cinti et al., 2011; Falcucci et al., 2011; Galli et al., 2008, 2012, 2015; Moro et al., 2013). In the third case, we adopted the approach suggested by Field and Jordan (2015). The authors derive time-dependent, renewal-model earthquake probabilities for two cases: when the date of the last event is unknown, and for the case in which the last event has occurred before historical record. This case is applied to the ISS numbers 14 and 25 in Figure 4. As suggested by Field and Jordan (2015), we computed the ratio between the integral of the BPT conditional probability curve (constrained by the historical completeness, Figure 4, solid curve) and the Poisson probability (Figure 4, dashed line). The historic open interval starts 717 years ago, as in this area the historical catalog of earthquakes is complete for M_w higher than ~ 6 starting from 1300 CE (Stucchi et al., 2011). The ratio is then used to multiply the Poisson probability in order to obtain a renewal time-dependent probability of occurrence for the next 50 years.

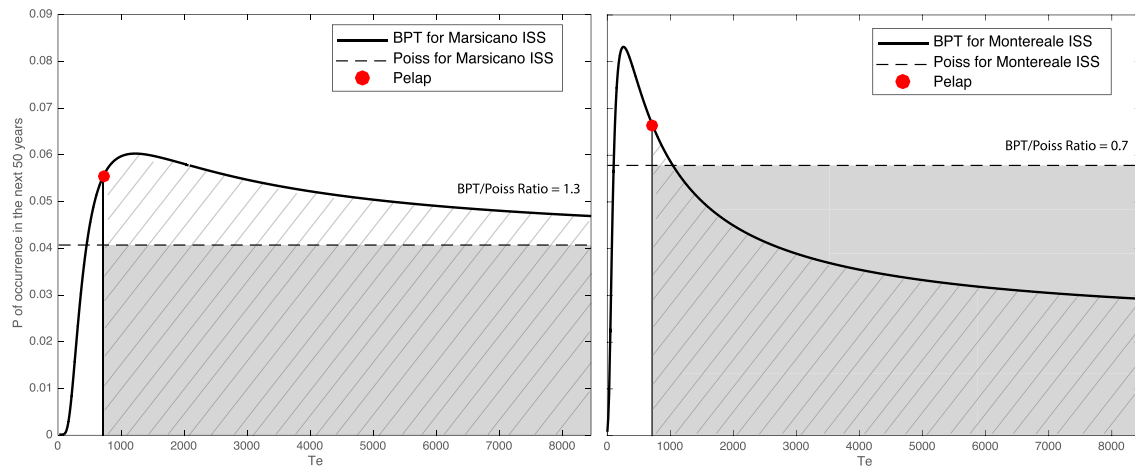


Figure 4. BPT and Poissonian probability of occurrence in the next 50 years for Marsicano and Montereale ISS. The red dots are the time-dependent probability of occurrence computed in the next 50 years, given an elapsed time of 717 years (minimum value computed from the open interval according to completeness criteria). The light gray and dashed areas are the parts of the distributions used to compute the ratio. ISS = individual seismogenic source; BPT = Brownian Passage Time.

3.1.3. The Expected Seismicity Rate and MFD Choice

Once all of these parameters have been investigated for each fault, we were able to calculate the seismic moment rate corresponding to M_{\max} and the MFDs of expected seismicity. In this study we used two MFD models: (i) a time-dependent *CHBPT* model (Eq. (1)), a symmetric Gaussian curve (applied to the incremental MFD values) centered on the M_{\max} value of each fault with a range of magnitudes equal to 1-sigma that allows the renewal process to begin again when the elapsed time since the last maximum sized event is known, and (ii) a *TGR* model (equation (2), Ordaz & Reyes, 1999; Kagan, 2002), with a minimum moment magnitude threshold equal to 5.5 and a $M_{\max} + 1$ standard deviation as the upper threshold for all sources. The considered b value is equal to 1.0 for all faults. This value corresponds to the mean b value determined from the CPTI15 catalog, as single-source events are insufficient for calculating the required statistics. Balancing the total MFD expected seismic moment rate with the seismic moment rate that was obtained based on M_{\max} and T_{mean} (details in Field et al., 1999; Field et al., 2015; Pace et al., 2016; Woessner et al., 2015), we calculated activity rates at magnitudes given by each MFD. We relied upon on the earthquake-source associations (Table 1) to assign an appropriate MFD to each fault: if at least one earthquake assigned to a fault source has a magnitude lower than the magnitude range in the curve of the *CHBPT* model distribution, the *TGR* model was applied to that fault source, otherwise a *CHBPT* model was used. Moreover, if a fault source has no associated earthquakes, we used a *CHBPT* MDF because we assumed that the mean recurrence time of that fault is similar to the characteristic behavior of a given fault in central Italy. It is worth noting that, even if based on neotectonic, palaeoseismologic, and seismotectonic data (see references in Table 1), the final seismogenic source model is a sort of expert judgment model.

3.2. Distributed Seismicity Input

The absence of surface ruptures associated with M_w lower than 5.5 earthquakes, the possibility of the earthquakes on blind or unknown faults and the impossibility to identify a causative source for important earthquakes in the historical catalog, forced us to take into account also distributed earthquakes into the final seismic hazard model. Following the approach developed in Valentini et al. (2017), which is based on the standard methodology developed by Frankel (1995), we estimated the density of seismicity in a grid with latitudinal and longitudinal spacing of 0.05° . We used the historical catalog of earthquakes (CPTI15; Rovida et al., 2016; Figure 1) to model the occurrence of earthquakes with magnitude higher than 4.5. With more than 4,000 events, the full catalog covers above the last thousand years from 1005 to 2014. Following Valentini et al. (2017) we first removed all the events considered as aftershocks via a declustering filter (Gardner & Knopoff, 1974) and all the events out of the completeness time windows (Stucchi et al., 2011). Moreover, in order to avoid double counting due to the use of two seismicity sources, we removed events associated with known active faults. The association of instrumental earthquakes with the active faults is

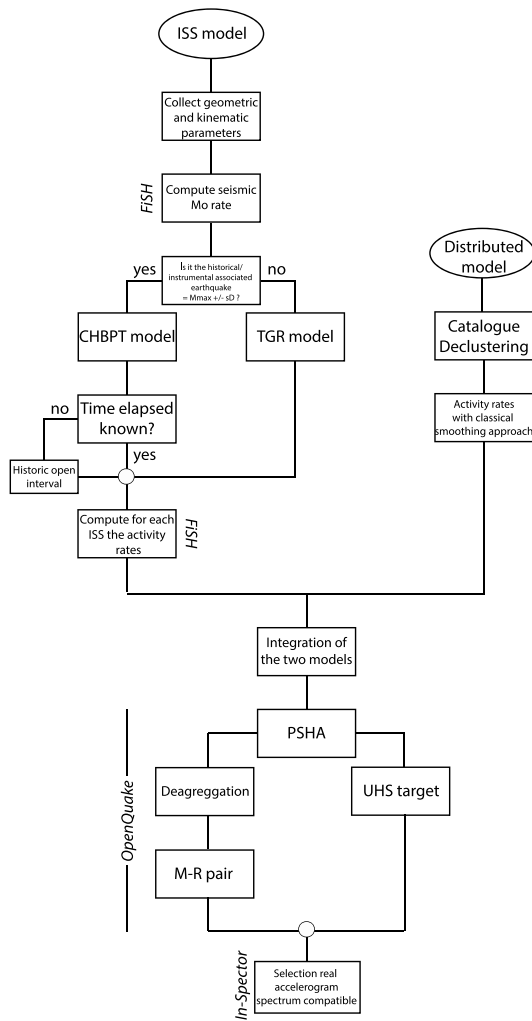


Figure 5. Flowchart that illustrates how, starting from a fault-based model, we select the real accelerogram spectrum compatible. ISS = individual seismogenic source; TGR = Truncated Gutenberg-Richter; CHBPT = CHaracteristic Gaussian Brownian Passage Time; PSHA = Probabilistic Seismic Hazard Analysis; M-R = magnitude-distance; UHS = uniform hazard spectrum.

controlled by the distribution of the aftershock sequences of the last ~30 years seismic events, whereas the association of historical records is based on the analysis of the distribution of the highest intensity data points. This process resulted in a catalog composed of 1,839 independent events. The smoothed rate of events in each cell i was determined as follows:

$$n_i = \frac{\sum_j n_j e^{-\frac{\Delta_{ij}^2}{c^2}}}{\sum_j e^{-\frac{\Delta_{ij}^2}{c^2}}} \quad (4)$$

where n_i is the cumulative rate of earthquakes with magnitudes greater than the completeness magnitude M_c in each cell i of the grid and Δ_{ij} is the distance between the centers of grid cells i and j . The parameter c is the correlation distance. The sum is calculated in cells j within a distance of $3c$ of cell i . The optimal smoothing distance c , that is, 30 km, is obtained by the probability gain per earthquake (Helmstetter et al., 2007; Kagan & Knopoff, 1977) for each pair of learning and target catalogs. The b value of the GR distribution is calculated following the approach recently proposed by Kamer and Hiemer (2015); we used a penalized likelihood-based method for the spatial estimation of the GR b values based on the Voronoi tessellation of space without tectonic dependency. The maximum magnitude M_{max} assigned to each node of the grid, the nodal planes, and the depths have been taken from European Seismic Hazard Model (Woessner et al., 2015). Following their approach the M_{max} has been anchored to the larger value between the largest earthquake reported in the catalog and the maximum magnitude expected based on the fault database, with proper consideration of its uncertainty, but not considering the arbitrary 0.2 increments proposed by European Seismic Hazard Model. Finally, the rates of expected seismicity for each node of the grid are assumed to follow the TGR model (Kagan, 2002).

3.3. Final Seismic Hazard Model

In order to treat the two source models as complementary models, we combined them into a single seismic hazard model, assuming that around a master fault there is a buffer area where no more than one single major fault is likely to be developed; the width of the buffer depends on the fault length and slip rate (Valentini et al., 2017). Into this buffer area the activity rate of the distributed model increases linearly from 0 (edge of the ISS)

to 1. All the steps followed in this work, starting from the definition of the two seismic models up to the ground motion selection, are summarized in the flowchart in Figure 5.

In Figure 6, we show the annual cumulative MFD computed for the distributed seismicity input, for the ISS input, their sum (Total in Figure 6), and for the CPTI15 catalog. Both distributed seismicity input and CPTI15 catalog MFD have been computed for the gray area shown in Figure 6. From moment magnitude equals 4.5 to 5.5 the historical catalog is fully described by the distributed seismicity input. Starting at $M_w = 5.5$, the annual cumulative rates of our model take into account also the contribution of the ISS model. The sum of the two models, the black solid line in Figure 6, which represents the total annual cumulative rates for our model, matches quite well the observed annual cumulative rate obtained using the catalog, at least until $M_w 6.7$. The biggest discrepancy between the total MFD and the CPTI15 MFD is given around $M_w = 7.0$. This discrepancy suggests that the completeness time window (~ 700 years), used to compute the annual cumulative rates for M_w higher than 6.8, is longer but not computable from the catalog, and so this can provide an overprediction of the rate at that magnitude for CPTI15. Once obtained the MFDs shown in Figure 6, we selected three ground motion prediction equations (GMPEs) to probabilistically obtain ground shaking for the study area. The GMPEs used in this work are (i) Bindi et al. (2011), (ii) Cauzzi et al. (2015),

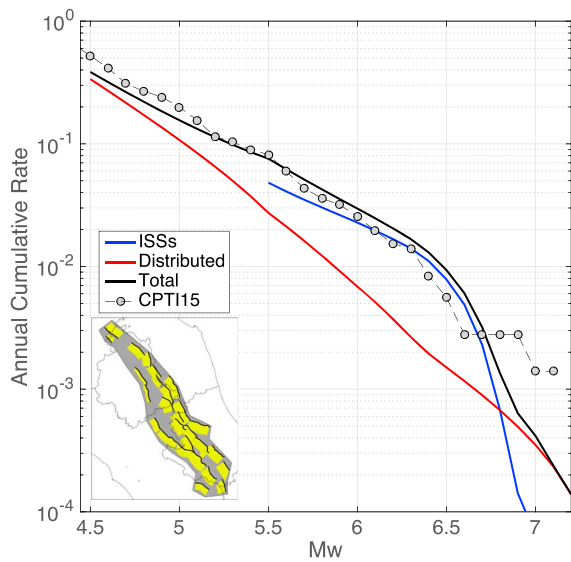


Figure 6. Annual cumulative MFD computed for the gray area. The rates have been computed using (i) the all ISSs listed in Table 2 (blue line), (ii) the distributed seismicity input (red line), summing ISS and distributed seismicity inputs (black line), and (iv) the full CPTI15 catalog. ISSs = individual seismogenic sources; MFD = magnitude-frequency distribution.

and (iii) Bindi et al. (2014), combined into a logic tree with the weights equal to 0.39, 0.27, and 0.34, respectively. The choice of these GMPEs and their relative weights comes from the selection and ranking of the GMPEs for the new Italian hazard map (Lanzano et al., 2017). In this work, the authors applied the method based on the log-likelihood value (Scherbaum et al., 2009) and two novel methods commonly used for general probabilistic forecasts (Gneiting & Raftery, 2007; Zechar & Zhuang, 2014). The data set used to select and rank the GMPEs includes more than 4,000 waveforms recorded by more than 1,000 strong motion stations relative to 137 events, among which the events of the 2016 seismic sequence. Although the first three scored GMPEs are different from the ones selected for our purpose, to explore the possible impact of the different distance metrics used in the GMPEs in the seismic hazard model, we selected the above mentioned GMPEs because they used three different distance metrics: (i) Joyner-Boore distance (R_{jb}), (ii) closest rupture distance (R_{rup}), and (iii) hypocentral distance (R_{hypo}), respectively, and also because they will be the three GMPEs used in the new Italian hazard map (Meletti et al., 2017).

All the computations are made using the OpenQuake Engine (Pagani et al., 2014), considering the ISS as *simple fault* source, and so the geometry description of the source is obtained by projecting the fault trace (i.e., a polyline) along the defined dip direction and the ruptures with a surface lower than the whole fault surface are floated so as to cover as much as possible homogeneously the fault surface.

In Figure 7 are shown the results expressed in terms of peak ground acceleration (PGA) for 10% and 2% of probability of exceedance (poe) in the next 50 years (since 2017), corresponding to return periods of 475 and 2,475 years. Areas with hazard levels greater than 0.30 g and 0.60 g at 50-year exceedance probabilities of 10 and 2%, respectively, are located in the central part of the study area and in the southern part. The

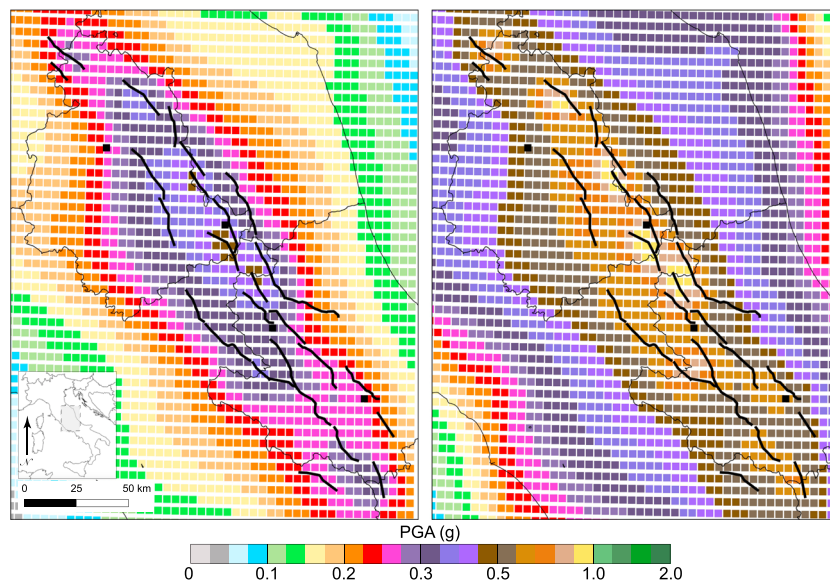


Figure 7. Seismic hazard maps expressed in terms of expected exceeded PGA for the study area. On the left, the map computed for 10% probability of exceedance in the next 50 years since 2017, and on the right the map computed for 2% probability of exceedance in the next 50 years since 2017, corresponding to return periods (T) of 475 and 2,475 years, respectively. The black lines are the ISSs traces, and the black squares are the location of the four analyzed sites. PGA = peak ground acceleration.

highest values of PGA are located nearby Norcia, in the central part of the study area, and these values range between 0.45–0.50 g and 0.90–1.0 g at 50-year exceedance probabilities of 10% and 2%, respectively.

4. Site-Specific Ground Motion Analysis

4.1. Deaggregation

Computation of target spectra requires deaggregation to identify which ISS and magnitude most contribute to the hazard for each site. Because multiple input sources and GMPEs were used in the total PSHA, deaggregation was extended to include the relative contributions of magnitudes and GMPEs to the computation of a target spectrum for ground motion selection. This section will discuss the issues associated with obtaining this deaggregation and using it to perform target spectrum calculations.

Figure 8 depicts the hazard curves at four sites, where deaggregation analysis was performed, aimed at identifying the M-R pairs that gave the highest contribution to the PGA values at probabilities of exceedance of 10% and 2% in the next 50 years (since 2017). We investigated also the impact of epsilon (ϵ), defined as the number of standard deviations from the median ground motion as predicted by an attenuation equation (Bazzurro & Cornell, 1999), and because these parameters did not affect the results (Figures S1 in the supporting information), we decided to perform all analysis with the value of 3ϵ . In this figure, we also show the contribution to hazard of the ISSs and distributed seismicity. It is important to note the different relative contribution of fault (ISS) and distributed seismicity to the total hazard, at the different levels of probability of exceedance. In the same Figure 8, we also show the contribution of each single fault source to the hazard of that site. Except for Perugia that will be discussed later in detail, the ISS input returned a larger contribution than distributed seismicity. This is mainly due to the location of the selected sites within the fault system (Figure 1). For the probability of exceedance of interest, we observed in Figure 8 that the ISSs that provide the main contribution to hazard in the selected municipalities are Nottoria-Preci (ISS 12) for Norcia; Campo-Felice (ISS 20) and Pizzoli-Pettino (ISS 15) for L'Aquila; and Sulmona (ISS 18) for Sulmona. We analyzed the contribution to the total hazard at these sites for the three GMPEs used. In Figure 9, in the insets where we show only the ISSs that contribute for a minimum of 10% of the total hazard with at least one GMPE, it is clear that the fault source contribution to the total hazard is modulated by the GMPEs and exposure time, but few ISSs drive the results. Once we have identified the fault source that mainly contributes to the total PGA at the selected sites, we performed the same analysis for SA of 1.0 and 2.0 s. The results (Figures S2 in the supporting information) show that the contribution did not significantly change. Because fault sources identified by the deaggregation analysis were characterized by different MFD, we also calculated the joint conditional distribution of magnitudes that caused the annual rate of exceedance of the SA level of interest. Figure 10 shows the normalized contributions in magnitude bins, only for the two ISSs for each site that shows the highest contribution in Figure 9: for L'Aquila, Norcia, and Sulmona, namely, the ISSs 15 and 20; 12 and 13; and 18 and 19, respectively. In Figure 10 we observe that magnitudes contribute to the total hazard, depending on the chosen MFD (CHBPT or TGR). In Norcia, for example, the ISS 12 has an associated TGR MFD; more than 30% normalized contribution (black dotted line) was given by magnitude between 5.5 and 6.5 if we consider the PGA at 10% of poe in 50 years. The same happens at 2% of poe in 50 years but the range is wider, between 5.5 and 6.8. Instead, for the ISSs that have an associated CHBPT MFD, the highest contribution was given by the central value of the CHBPT MFD (M_{\max} in Table 3) if the site is located within the projection on the surface of the fault plane, as for ISS 18 in Sulmona, and by the central value $+0.1$ if the site is located outside the projection on the surface of the fault plane, as for ISSs 20 and 15 in L'Aquila. With these criteria (i.e., magnitude bins that contribute more than 30%) we selected the magnitude range as input for target spectrum selections (Table 4).

A range of epicentral distances was obtained assuming that earthquakes on normal faults mostly nucleate on the deepest part (lower half) of the fault (Harris, 2003; Scholz, 1988; Sibson, 1983, 1989, 2003). In order to define the epicentral distances for the accelerograms selection, we arbitrarily assumed three possible nucleation points, corresponding to a bilateral rupture from a nucleation point near the deep central part of the fault, and two unilateral ruptures from nucleation points located close to the deep lateral tip of the fault (Figure 9a). It is important to highlight that the hypothesized nucleation points do not correspond to the OpenQuake modeling but have been used only for the accelerograms selection purpose. For the Perugia municipality the fault source input returned a lower contribution than the distributed seismicity

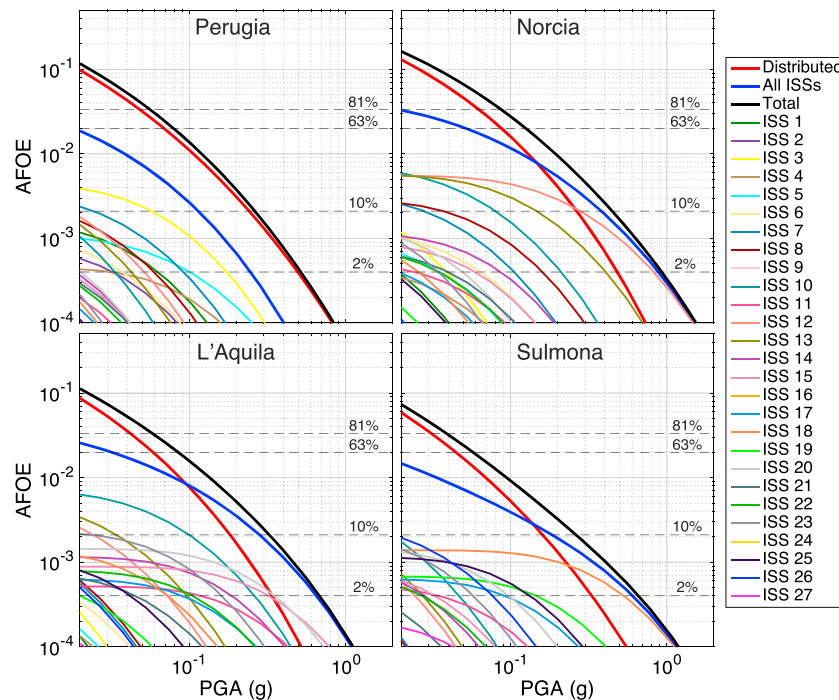


Figure 8. Hazard curves for the four investigation sites. The red, blue, and black lines represent the hazard curves for the distributed seismicity input, ISS input, and the total, respectively. The others lines (from ISS 1 to ISS 27) represent the hazard curves of each ISS. The dashed horizontal black lines represent the value of annual frequency of exceedance (AFOE) for different probability thresholds of exceedance in the next 50 years since 2017. ISS = individual seismogenic source; PGA = peak ground acceleration.

(Figure 8), and for this reason, we performed a classical deaggregation analysis, using only the distributed seismicity input, to obtain the M-R pairs. The results in Figure 11 show that the highest contribution was given by $M_w = 5.75$ and $M_w = 6.25$ at 10% and 2% of poe, respectively, and for distances smaller than 15 km. Moreover, because for a given event, the magnitude can change according to the database used for the selection, (e.g., for the 2009 L'Aquila earthquake, M_w 6.1 and M_w 6.3 are reported in the European Strong Motion (ESM), <http://esm.mi.ingv.it>, and in the Pacific Earthquake Engineering Research center (PEER), <https://ngawest2.berkeley.edu/>, databases, respectively), we enlarged the magnitude ranges of 0.2 for both minimum and maximum magnitude values to take into account the uncertainties in magnitude assignment. The M-R pairs used for the selection of real recorded accelerograms, for each municipality, are listed in Table 4.

4.2. Definition of Seismo- and Spectrum-Compatible Ground Motions

In this section, we show the procedure followed for the selection of a set of real recorded accelerograms, suitable for input motion of site response analyses in the representative sites here considered. According to the recommendations by international technical codes (Pagliaroli & Lanzo, 2008), a set of seven signals was considered. These analyses can be used for the definition of seismic input in the design of structures as well as for level-3 SM studies. The choice of the real recorded accelerograms is related to a good knowledge of the seismotectonic context and seismic hazard of the site, which controls the magnitude, distance, and kinematics of the seismogenic sources that mostly contribute to the hazard. Furthermore, according to the Italian building code (NTC, 2018), the accelerograms have to be compatible with the elastic response spectra of the site. The matching criterion applies to the average 5% damped elastic response spectrum of selected time histories; this spectrum should have no value lower than 90% and higher than 130% of the corresponding value of the target spectrum. This criterion must be satisfied in the period range of interest.

The elastic response spectra used here as target spectrum in the selection of the real recorded accelerograms are the UHS related to a 10% probability of exceedance of the PGA in 50 years (means a recurrence time,

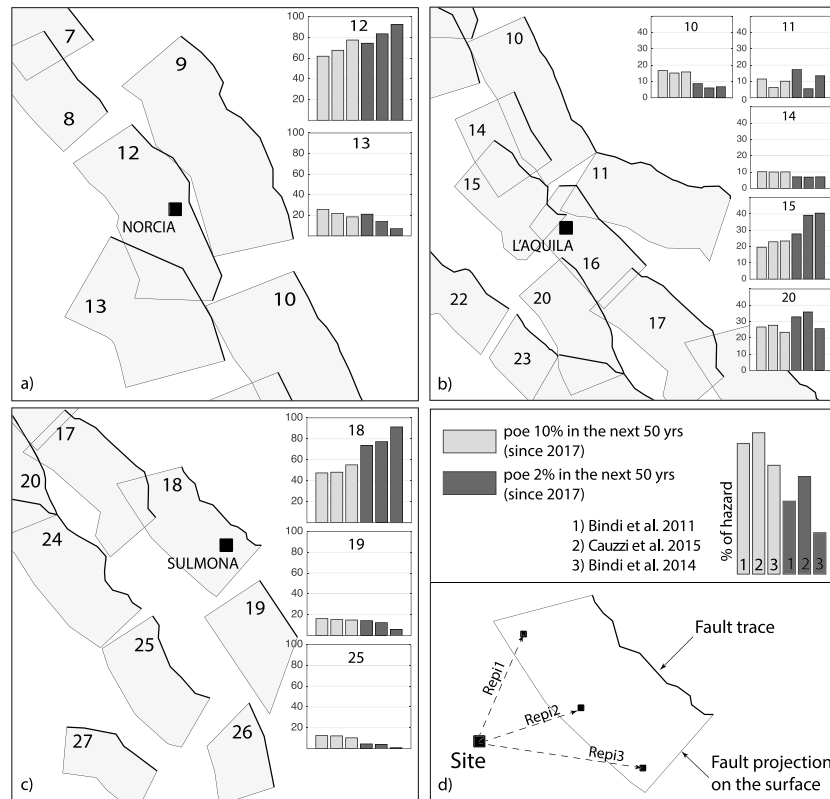


Figure 9. (a–c) Deaggregation results for Norcia, L'Aquila, and Sulmona sites. For each site are shown only the ISSs that contribute for a minimum of 10% of the total hazard with at least one GMPE. In light gray and dark gray are shown the deaggregation results for 10% and 2% of probability of exceedance in the next 50 years since 2017, respectively. (d) Sketch to explain the distances used to define the M-R pairs. ISSs = individual seismogenic sources; GMPE = ground motion prediction equation; M-R = magnitude-distance; poe = probability of exceedance.

$T_r = 475$ years), obtained from the PSHA described in section 3. The considered return period (475 years) is the value usually adopted for the ultimate limit state design of ordinary structures as well as for the seismic input in level-3 SM studies (Pagliaroli, 2018). The target spectra were calculated for the four sites of Perugia, Norcia, L'Aquila, and Sulmona. Using the M-R pairs listed in Table 4, we preselected a number of real recorded accelerograms (only the horizontal component) of normal faulting earthquakes in the ESM (<http://esm.mi.ingv.it>) and PEER center (<https://ngawest2.berkeley.edu/>) databases. We selected only recordings at outcropping rock or very stiff soil (i.e., $V_{s30} \geq 700$ m/s) conditions. This choice (i.e., choosing 700 m/s instead of 800 m/s defined as the lowest limit for rock or stiff soil condition by Norme Tecniche per le Costruzioni) allows to significantly expanding, at least for Italian database, the number of available recordings avoiding sites with significant site effects. As matter of fact, recordings sites characterized by V_s in the range 700–800 are usually jointed-weathered rock sites.

Moreover, as evident in Table 4, distances from the modeled source of sites are generally shorter than 20 km. In these near-source conditions, ground motions and seismic structural response may show spatial variability different from far-source conditions (Chioccarelli & Iervolino, 2014). Among other works, Iervolino et al. (2017) indicated that pulse-like records constitute one of the causes of such spatial variability. In particular, Iervolino et al. (2017) indicated that rupture directivity is the most prominent causal mechanism of impulsive ground motion. Such impulsive behavior of near-source ground motions has been found in Italian seismic events of normal faulting style (e.g., Chioccarelli & Iervolino, 2010; Iervolino et al., 2017). Since Bertero et al. (1978), pulse-like records have been identified and constitute a particular category of seismic input, whose engineering importance regards how the ground motions can subject ductile structures to greater inelastic displacements, on average, with respect to nonimpulsive seismic input (e.g., Iervolino et al., 2012). For the intrinsic characteristics of the pulse-like record, their relative scarcity in records of ground

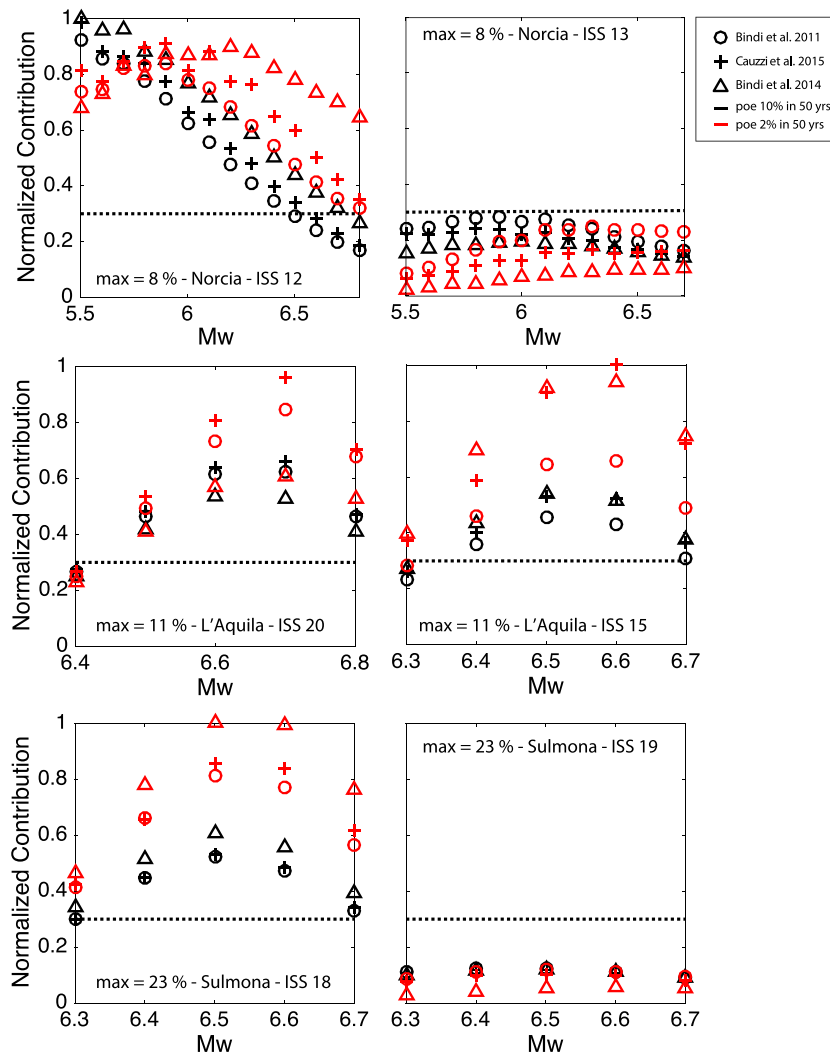


Figure 10. Deaggregation analysis performed for each bin of magnitude for the two ISSs that mostly contribute to the hazard for the three sites in Figure 9. The red and black markers are for PGA at 2% and 10% probability of exceedance in the next 50 years (since 2017). The different markers (triangle, circle, and cross) indicate the different GMPEs. The dotted black lines represent the 30% of the normalized contribution to the hazard. All values were normalized by the maximum percentage contribution, given within each graph. ISSs = individual seismogenic sources; GMPEs = ground motion prediction equations; PGA = peak ground acceleration.

motion databases can be attributed to a not adequate density of accelerometric network spanning the epicentral area. In recent years, modern seismic networks furnished new data on recorded seismic events nucleating in the near field (e.g., Parkfield, California, 2004; L'Aquila, Italy, 2009; and Amatrice, Italy, 2016), providing evidence of impulsive recordings. To account for such particular seismic effects, we identified a set of 20 ground motions being identified as pulse like. We used this ground motion set to integrate the analyzed registration data set.

Table 4

M-R Pairs Used to Select the Real Recorded Accelerograms

Site	Latitude	Longitude	M_w min	M_w max	Repi min (km)	Repi max (km)
L'Aquila	42.350	13.390	6.1	7.0	9.5	29
Norcia	42.790	13.100	5.3	6.6	5.8	11.7
Perugia	43.110	12.390	5.55	5.95	5	15
Sulmona	42.050	13.930	6.1	6.9	7.8	20.5

Note. The M_w range is evaluated for the 10% of probability of exceedance in the next 50 years since the 2017. For the definition of Repi see the Figure 9. M-R = magnitude-distance.

Overall, we analyzed, for the four sites, 106 registrations divided into (i) Perugia: 18 registrations for 7 different events, (ii) Norcia: 34 registrations for 13 different events, (iii) L'Aquila: 32 registrations for 4 different events, and (iv) Sulmona: 22 registrations for 3 different events. Then, for each site, we selected seven spectrum-compatible accelerograms using the procedure proposed by Pagliaroli and Lanzo (2008) by employing the *In-Spector* software (Acunzo et al., 2014):

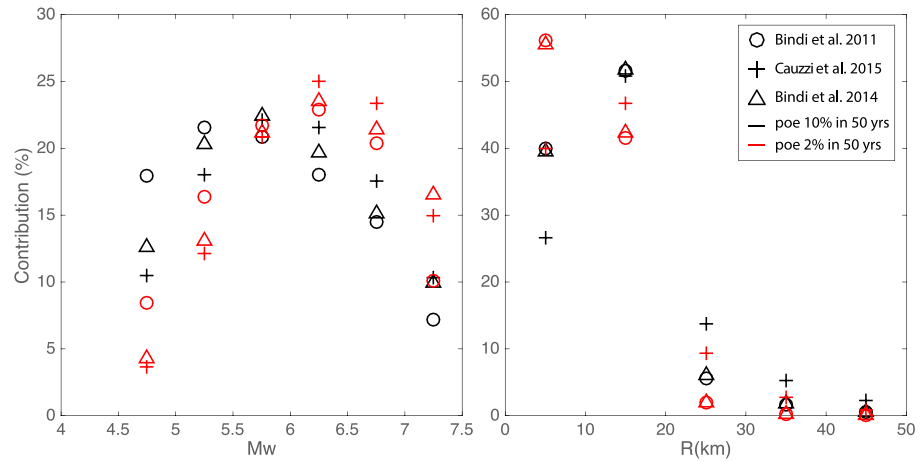


Figure 11. Results from classical deaggregation performed only for Perugia site. The red and black markers are for the 2% and 10% of poe in the next 50 years (since 2017). The different markers (triangle, circle, and cross) indicate the different GMPEs. GMPEs = ground motion prediction equations; poe = probability of exceedance.

1. All candidate records were first scaled to the target PGA applying a constant scaling factor (SF). Records characterized by SF higher than 4 or lower than 0.25 were rejected.
2. Check of the spectrum compatibility of each recordings using the D_{RMS} parameter as defined in Bommer and Acevedo (2004):

$$D_{RMS} = \frac{1}{N} \sqrt{\sum_{i=1}^N \left(\frac{SA_0(T_i)}{PGA_0} - \frac{SA_S(T_i)}{PGA_S} \right)^2} \quad (5)$$

where N is the number of periods where the spectra are specified, $SA_0(T_i)$ is the SA of the selected accelerogram at the period T_i , $SA_S(T_i)$ is the SA of the target spectrum at the same period, PGA_0 and PGA_S are the accelerogram PGA and the target spectrum anchor point. The D_{RMS} parameter was computed in the period range selected by the user, which in our case is between 0.1 and 1.0 s, which comprise the fundamental periods of the large part of structures in the selected sites (i.e., masonry/concrete few-story buildings). The lower is the D_{RMS} the better is the compatibility between the shape of the spectrum under consideration and the reference shape. According to this step, preference was given to recordings characterized by minor values of D_{RMS} . Note that the maximum exceedance of an individual record from the target spectrum is an important issue as this deviation can impose an exceptionally high and unrealistic demand for structural and geotechnical systems.

3. Refinement of selection by applying additional preference criteria: (i) only one component of the same recording station, (ii) only one registration of the same event, and (iii) events from Italian extensional seismotectonic context, (iv) considering that the reference distance is in the order of 20 km, pulse-like recordings.
4. Final check on the compatibility of seven selected records with the target spectrum. The compatibility of the mean spectrum of seven accelerograms selected according to Steps 1–3 with the target spectrum was checked in the period range of interest. As compatibility criterion, it was assumed that no value of the mean spectrum calculated for all of the selected records should be less than 90% (see, for instance, CEN, 2004) of the corresponding value of the 5% damped target response spectrum in the period range of interest; if this requirement is not respected in some period ranges, single scaling factor is slightly varied, and/or one or more recordings are changed to achieve average compatibility.

All these rules allowed us to select the events and associated parameters listed in Table 5. It is worth noting that the choice of the seven spectrum-compatible accelerograms is not univocal and the user can select a different set of accelerograms provided these are selected following the procedure described above. The comparison between the response spectrum of the seven spectrum-compatible accelerograms, the mean spectrum, and the UHS target spectrum, for each site, is shown in Figure 12. The average spectrum

Table 5
Events and Associated Parameters for the Seven Real Recorded Accelerograms Selected for the Four Investigation Sites

ID	Station	Component	Country	Event	M_w	Repi (km)	SF	D_{RMS}	Vs30 or class site	Pulse like	Database
PERUGIA											
Pg1	ATN	E/O	Italy	05/07/1984	5.9	10.1	2.17	0.04	A	No	ESM
Pg2	CESM	E/O	Italy	10/14/1997	5.6	8.7	2.53	0.05	A	No	ESM
Pg3	CLO	N/S	Italy	10/26/2016	5.9	10.8	1.26	0.04	A	Yes	ESM
Pg4	CSC	N/S	Italy	09/19/1979	5.8	9.3	1.55	0.05	700	Not-inv.	ESM
Pg5	SLO	E/O	Italy	10/26/2016	5.9	14.4	4.00	0.04	A	No	ESM
Pg6	CSC	E/O	Italy	09/19/1979	5.8	9.3	1.15	0.04	700	Not-inv.	ESM
Pg7	AQK	N/S	Italy	04/06/2009	6.3	5.4	2.93	0.06	700	Yes	PEER
NORCIA											
No1	ATN	E/O	Italy	05/07/1984	5.9	10.1	3.75	0.04	A	No	ESM
No2	CLO	N/S	Italy	10/26/2016 (2)	5.9	10.8	2.18	0.04	A	Yes	ESM
No3	CSC	N/S	Italy	09/19/1979	5.8	9.3	2.15	0.05	700	Not-inv.	ESM
No4	T1212	N/S	Italy	10/30/2016	6.5	10.5	1.51	0.05	A	No	ESM
No5	NUS	000	Italy	10/06/1997	5.5	12.5	2.58	0.03	A	Not-inv.	PEER
No6	CLO	N/S	Italy	10/26/2016 (1)	5.4	10.8	3.29	0.04	A	No	ESM
No7	3506	N/S	Turkey	12/16/1977	5.3	9.5	1.06	0.07	770	Not-inv.	ESM
L'AQUILA											
Aq1	MRNA	HN3	Greece	06/15/1995	6.5	16.6	4.0	0.07	-	Not-inv.	ESM
Aq2	CSC	N/S	Italy	10/30/2016	6.5	14.9	1.86	0.05	700	Yes	ESM
Aq3	MMO	E/O	Italy	10/30/2016	6.5	19.2	1.56	0.04	A	No	ESM
Aq4	MNF	E/O	Italy	10/30/2016	6.5	26	2.21	0.05	A	Yes	ESM
Aq5	T1212	N/S	Italy	10/30/2016	6.5	10.5	1.05	0.05	A	No	ESM
Aq6	T1213	E/O	Italy	10/30/2016	6.5	12	3.39	0.07	A	Yes	ESM
Aq7	AQK	N/S	Italy	04/06/2009	6.3	5.4	0.81	0.04	700	Yes	PEER
SULMONA											
Su1	MRNA	HN3	Greece	06/15/1995	6.5	16.6	3.66	0.03	-	Not-inv.	ESM
Su2	ACC	E/O	Italy	10/30/2016	6.5	18.6	0.57	0.05	A	Yes	ESM
Su3	CSC	N/S	Italy	10/30/2016	6.5	14.9	1.56	0.05	700	Yes	ESM
Su4	T1213	E/O	Italy	10/30/2016	6.5	12.0	0.88	0.11	A	Yes	ESM
Su5	T1215	N/S	Italy	10/30/2016	6.5	20.1	2.76	0.06	A	No	ESM
Su6	AQG	E/O	Italy	04/06/2009	6.3	6.8	0.51	0.05	700	Yes	PEER
Su7	AQK	E/O	Italy	04/06/2009	6.3	5.4	0.73	0.04	700	Yes	PEER

Note. Vs30 is expressed in meter per second, the class site is according to EC8. *Not-inv* means that the recording was not investigated to assign or not the pulse-like behavior. ESM = European Strong Motion; PEER = Pacific Earthquake Engineering Research.

computed from selected accelerograms is very close to the target one verifying the compatibility requirements in the period range 0.1–1.0 s and with single deviations generally less than 30%.

5. Discussions

5.1. Fault Based Versus Cornell UHS

We compared our results of probabilistic fault-based and time-dependent seismic hazard model, in terms of UHS computed for 10% of probability of exceedance in 50 years with those of the classical Cornell (1968) approach obtained by the national Italian seismic hazard model (MPS04, Stucchi et al., 2011), currently used as reference model by the Italian building code (NTC, 2018). The comparison is shown in Figure 13, for the four selected sites.

With respect to those computed by MPS04, the UHS obtained in this study is more severe for the sites of Norcia, Perugia, and L'Aquila, whereas are less severe for the Sulmona site (Figure 13a). In Figure 13b, we show the ratio between the UHSs computed in this study and those computed by MPS04. For all the four sites, this ratio is greater than 1 for PGA and periods up to 0.25 s. These ratios tend to decrease from 0.25 to ~0.3 s–0.5 s. In this range, except the Norcia site, the ratios are generally lower or equal to 1. At periods longer than ~0.7 s, except Perugia site, the ratios tend to be approximatively constant, ranging between ~1.2 and 0.8. The UHS ratio for Perugia shows, instead, an increase in the range from ~0.7 to 1.5 s, at 1.5-s reaches and maintains a value of ~1.2 till to 2 s.

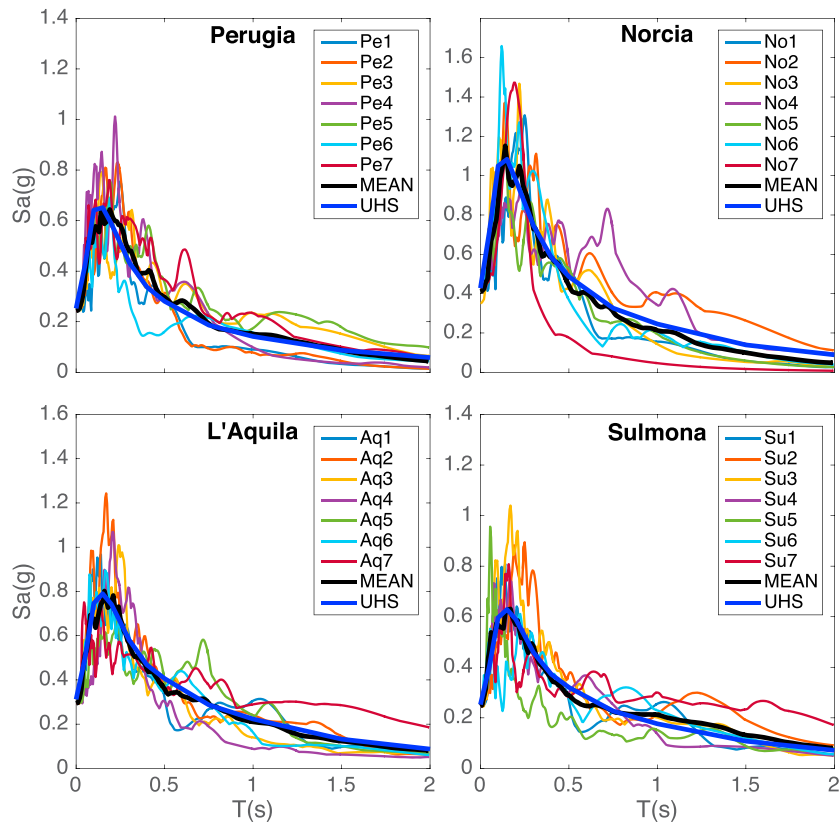


Figure 12. The seven real recorded spectra selected using the M-R pairs described in the paper for the four site investigations (thinner lines with different colors). The black line is the mean spectrum computed by inspector from the seven selected spectra. The blue line is the uniform hazard spectrum obtained through the hazard analysis described in section 3, for a return period of 475 years, and used as target spectrum in the selection of the seven real recorded spectra. The seven real accelerograms selected for each site (Table 5) are given in the supporting information. M-R = magnitude-distance; UHS = uniform hazard spectrum.

The differences between UHS obtained in this study with those provided by MPS04 may be related to (i) the different GMPEs adopted and (ii) the different approaches and input data used to perform PSHA. Meletti et al. (2016) show that recent GMPEs produce higher hazard estimates with respect to those adopted by

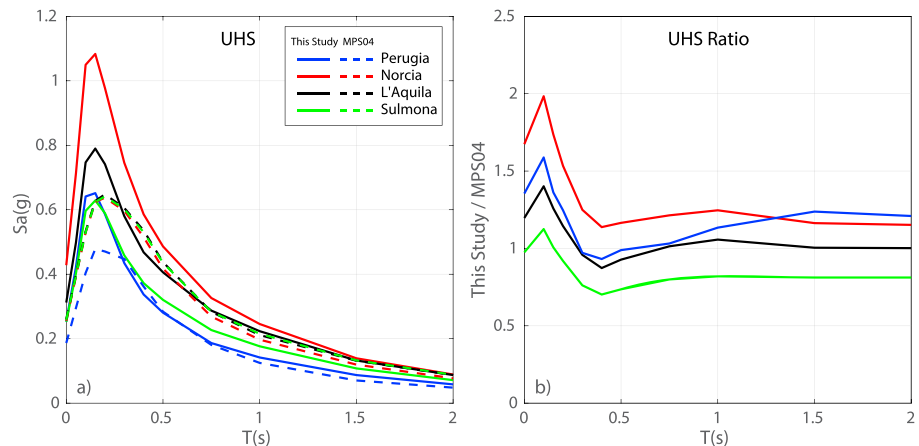


Figure 13. Comparison of the UHS computed in this study and UHS from MPS04 (Stucchi et al., 2011) for the four sites investigated; (a) UHS for the 10% of probability of exceedance in 50 years; (b) ratio between the UHS from this study and the UHS from MPS04. UHS = uniform hazard spectrum.

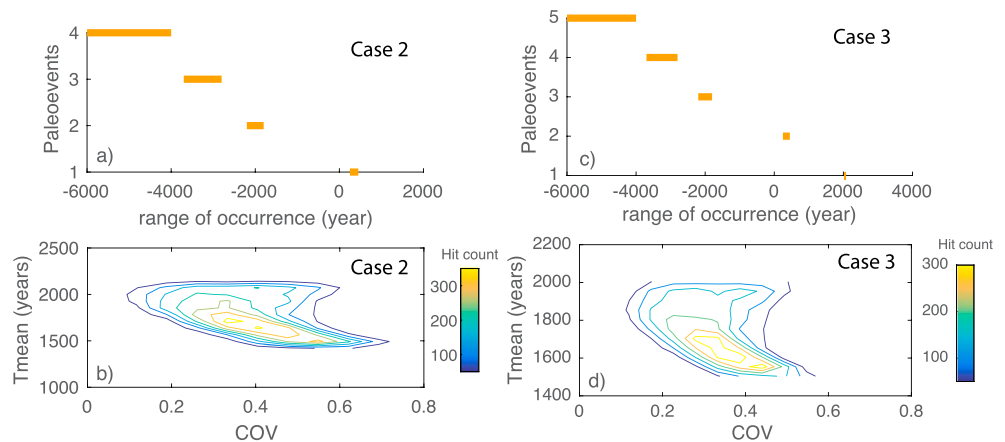


Figure 14. Comparison of recurrence parameters for ISS9 Bove-Vettore: (a and c) Paleoseismological data used to compute the T_{mean} and the CoV for the Cases 2 and 3, respectively. (b and d) Results from Monte Carlo simulation performed to compute the T_{mean} and the CoV for the Cases 2 and 3, respectively. CoV = coefficient of variation.

MPS04 and clue that the possible reasons are the larger values of uncertainty (standard deviation) with respect to older GMPEs (e.g., Bommer and Abrahamson, 2006), as well as the inclusion of recordings in the near field, that were lacking in previous GMPEs used for the MPS04 model. According to Meletti et al. (2016), we observed the highest differences between the recentmost UHS obtained in this study and those obtained in MPS04, in the range of period from PGA to 0.3 s.

The differences in the UHSs are also affected by the different approaches used to perform PSHA and the input data (CPTI04 in MPS04, CPTI15, and faults in this study). MPS04 used a classical Cornell approach, based on a seismogenic zone model. Basically, this means that the earthquake rates of each seismogenic zone are spread over it. The comparisons in Figure 13 confirmed that with a Cornell's approach, the spatial distribution and the relative values of the seismic hazard are controlled by the geometry of seismogenic zones; however, this effect could potentially mask significant spatial variations in the hazard, as reflected by historical seismicity and faults geometry and slip rates. The UHS computed by MPS04 for L'Aquila, Sulmona, and Norcia sites is almost similar to each other, and, effectively, these three sites fall inside the same seismogenic zone in the MPS04 model.

On the contrary, in this study, we modeled that future earthquakes are more likely to occur at sites near the epicenters of previous earthquakes, and, where a fault is known, are more likely to occur on that fault. This approach reveals a different spatial distribution and pattern of hazard estimates. In our fault-based model, the UHS is also controlled by two main factors: (i) the time elapsed from the last large earthquake occurred on faults and, (ii) the MFD associated to each fault. This approach implies that, for L'Aquila site, the seismic hazard, and the UHS, is not affected by the Paganica fault (which has an elapsed time of 9 years and a probability of occurrence of a next earthquake lower than $\sim 2e-09$). However, due to the presence in the surrounding area of a relevant number of known active faults, the resulting hazard is higher than the hazard evaluated for the Sulmona site, in spite of the Sulmona fault (ISS18) has $\sim 7\%$ probability of rupture in the next 50 years. Interestingly, the Norcia UHS is the highest among the four sites. We argue that this result is mainly controlled by the modeled MFD of the ISS 12-Nottoria-Preci, which is a TGR. The seismogenic parameters of this fault are similar to the ones used for the ISS 18 near Sulmona (Table 3), but with the difference that the MFD of the ISS 12 ranges from M_w 5.5 to M_w 6.8. We can argue that the contribution to the seismic hazard for 10% poe in 50 years is then strongly controlled by the occurrences of earthquakes in the range of M_w 5.5 to ~ 6 .

5.2. Remarks After the 2016 Central Italy Earthquake Sequence

The occurrence of the 2016 earthquake sequence motivated many seismological, seismotectonics, and paleoseismological studies, finalized to a better knowledge of the seismological sources in the area, regarding geometry, kinematics, seismic history, and seismogenic potential. The new data can improve the seismic hazard models, in particular fault-based and time-dependent approaches.

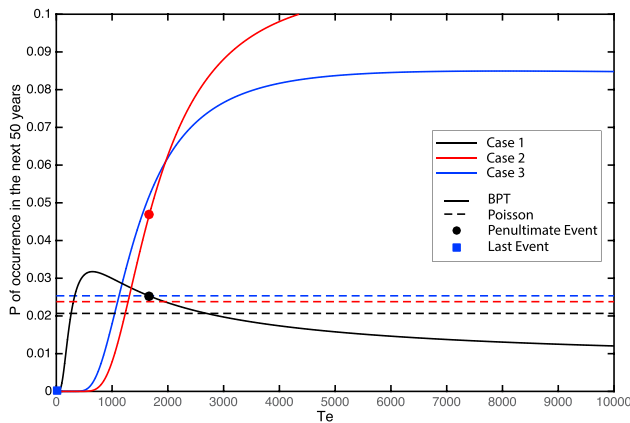


Figure 15. BPT and Poissonian probability curves versus elapsed time (T_e) calculated for the Bove-Vettore ISS9: The three cases explored in this study refer to (1) geometrical/kinematic parametrization of the source before the 2016 sequence ($T_{\text{mean}} = 1971$; $\text{CoV} = 1.24$); (2) use of paleoseismological data, excluding the 2016 event ($T_{\text{mean}} = 1710$; $\text{CoV} = 0.33$); (3) as (2) but including the last event ($T_{\text{mean}} = 1604$; $\text{CoV} = 0.39$). BPT = Brownian Passage Time; CoV = coefficient of variation.

In order to evaluate the impact of the new data collected after the 2016 seismic sequence, we compared the hazard in Norcia site considering only the ISSs in the surrounding of the area (ISS: 9, 10, 12,13) and taking into account the variations in the geometrical and kinematical parameters for the ISSs involved in the sequence (9-Bove-Vettore and 10-Gorzano). We evaluated three cases: (1) before the seismic sequence, (2) before the seismic sequence with the new knowledge, and (3) after the seismic sequence. In the first case, we used old geometrical and kinematical parameters (length, seismogenic thickness, rake, and long-term slip rate), from Valentini et al. (2017), to compute the activity rates for the two ISSs involved in the 2016 sequence. Being a time-dependent approach a key role is played by the time elapsed since the last event. In the first two cases the last event occurred on the Bove-Vettore source $\sim 1,700$ years ago (Table 1), whereas in the last case the elapsed time is only 1 year. Moreover, in Cases 2 and 3, we used new data acquired after the sequence, in particular the new paleoseismological data collected on the fault, to understand how a good knowledge of a fault seismic history impacts the hazard estimation. We used new paleoseismological data (Galli, Galderisi, et al., 2017) as input for the *FiSH* tool *Recurrence Parameters* (Pace et al., 2016) to calculate T_{mean} and CoV . Considering the reconstructed seismic history of the fault, *Recurrence Parameters* uses a Monte

Carlo approach, by performing n simulations of the earthquake catalog, with the age of each event randomly varying within its uncertainties. In total, 10,000 synthetic catalogs were computed, and T_{mean} and CoV were extracted from each of them (Figure 14). The CoV and T_{mean} computed without this approach, and so by the long slip rate variability (Case 1), are equal to 1.24 and 1971 years, whereas in the other two cases computed from paleoseismological data are equal to 0.33 and 1,710 years (Case 2), and 0.39 and 1604 years (Case 3). A different value of the CoV in a time-dependent approach means a different shape of the BPT curve and consequently a different probability of occurrence (Figure 15). The time-dependent probability of occurrence of a maximum earthquake on the Bove-Vettore fault in the next 50 years changes from $\sim 2\%$ to $\sim 5\%$, before the 2016 sequence (T_e since the penultimate event $\sim 1,700$ years) if we use an updated and complete paleoseismic history, and it drops off close to zero after the occurrence of the 2016 seismic sequence. It is worth noting that for the seismic hazard model proposed in this work, we used a CoV and T_{mean} computed by the long slip rate variability (similar to Case 1) for all ISSs. In particular, for the Bove-Vettore source, we inferred different values of CoV and T_{mean} (1.15 and 2042 years, respectively, see

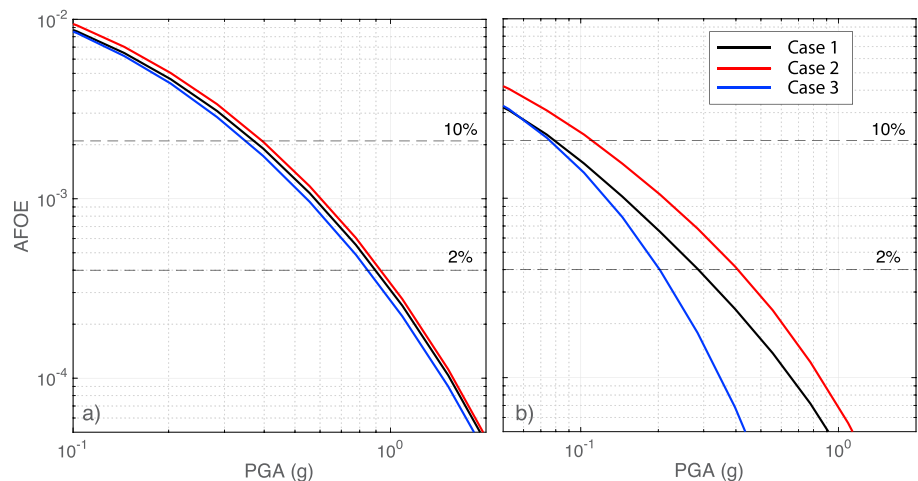


Figure 16. (a) Hazard curves computed at Norcia considering four ISSs (9, 10, 12, and 13) in the surrounding area. (b) Hazard curves computed at Norcia considering only the two ISSs (9 and 10) involved in the 2016 seismic sequence. All the hazard curves are computed for the three cases explored in this study. ISSs = individual seismogenic sources.

Table 3) from the ones computed in Case 1 because instead of using old geometrical and kinematical parameters we used the new ones.

Finally, in Figure 16 are shown the PGA hazard curves computed for Norcia for the three cases described above. In Figure 16a (obtained using the ISSs 9, 10, 12 and 13) the three hazard curves are only slightly different, because the ISS number 12 is the one that mostly contributes (almost 80%, see Figure 9) to the hazard for this site. The differences are in the order of 15% and 10% for the 10% and 2% of probability of exceedance, respectively, and the hazard curve computed for the second case is the highest. In Figure 16b, we removed the ISSs numbers 12 and 13 in order to highlight the differences due to the new data collected for the sources involved in the last sequence: 9-Bove-Vettore and 10-Gorzano faults. The figure shows clearly how a better knowledge of the source, especially in the paleoseismological data set, can have an important impact on the seismic hazard estimation. The figure shows also that in a fault-based PSHA, the time-dependent approach can play a key role in the hazard estimation. In the third case, where the elapsed time from the last earthquake is 1 year for ISS 9-Bove-Vettore, the hazard curve (after 2016 curve in Figure 16b) shows the lowest values as it is actually controlled mainly by the ISS 10-Gorzano.

6. Conclusions

In this study, we performed a fault-based and time-dependent probabilistic seismic hazard deaggregation analysis for four investigation sites (Perugia, Norcia, L'Aquila, and Sulmona) in central Italy, where a damaging seismic sequence in 2016–2017 occurred causing 299 casualties. We evaluated the sources, magnitudes, and epicentral distances that most contribute to the hazard of the sites. The results were used to select the M-R pairs for the selection of real strong motion data, from both pulse- and not pulse-like records.

We evaluated the impact in the PSHA of the fault-based and time-dependent approach, and of the new seismological, seismotectonic, and paleoseismological knowledge acquired after the seismic sequence. We compared the UHS from our study with the ones used in the Italian building code, and probabilities of occurrences and hazard curves before and after 2016 new data. From our study we have reached the following conclusions.

1. A fault-based and time-dependent approaches give a complementary view of PSHA with respect to zone-based and Poisson ones, especially in terms of spatial resolution and extension of the observational time required to capture the recurrence of large-magnitude events, improving the reliability of seismic hazard assessments.
2. The used approach allows exploring a wider range of M-R contribution to the hazard compared to the use of large seismogenic zones. In this latter case, in fact, significant contributions to probabilistic seismic hazard are almost exclusively due to possible earthquake locations closest to the site.
3. In a fault-based and time-dependent approaches, improving the knowledge of the seismogenic sources, regarding geometry, kinematics, seismic history, and seismogenic potential can have a large impact to final results and have to be carefully taken into account to avoid incorrect hazard estimates. To this aim, we encourage collecting and analyzing new geological data on active faults.
4. We suggest taking carefully into account in PSHA the variability of the ground motion in near source conditions; in our study we included some pulse-like records in the accelerograms selection.
5. Future efforts should focus on relaxing fault segmentation, considering the possibility of multisegment ruptures, and on better quantifying and reducing the uncertainties on some key parameters in fault-based PSHA, such as slip rates, mean recurrence times, and CoV.

Finally, in spite of limits and uncertainties of the approach, we suggest using this study as a guideline in the selection of strong motion registrations for numerical simulation in regions where the knowledge of the active faults is quite large.

References

- Acunzo, G., Pagliaroli, A., & Scasserra, G. (2014). In-Spector: Un software di supporto alla selezione di accelerogrammi naturali spettro-compatibili per analisi geotecniche e strutturali. *GNGTS*, 2, 107–114.
- Baker, J. (2011). Conditional mean spectrum: Tool for ground motion selection. *Journal of Structural Engineering*, 137(3), 322–331. [https://doi.org/10.1061/\(ASCE\)ST.1943-541X.0000215](https://doi.org/10.1061/(ASCE)ST.1943-541X.0000215)
- Barchi, M. R. (2010). The Neogene-Quaternary evolution of the northern Apennines: Crustal structure, style of deformation and seismicity. *Journal of the Virtual Explorer*, 36. <https://doi.org/10.3809/jvirtex.2009.00220>

Acknowledgments

The authors would like to thank the Associate Editor Laura Peruzza, Graeme Weatherill, and another anonymous reviewer for helpful comments and revisions that significantly improved the manuscript. We warmly thank Gian Maria Bocchini for his contribution during the very first part of the Project. This work was funded by an Agreement between Università “G. d’Annunzio” Chieti-Pescara and Regione Abruzzo called *Studi di pericolosità di base per la definizione di terremoti di riferimento* (B. Pace scientific responsible), by Fondi Dipartimento DiSPUTer (B. Pace and P. Boncio, responsible for “ex 60%” fund), and by the Italian Ministry of Education and Research (MIUR) funded CIPE-FISR2016-INGV project FISR4D-Musacchio. All the used parametric data for faults and earthquakes are reported in the tables and have been taken from published literature, listed in the references. The strong motion registrations selected for each investigation site are reported in supporting information S12. All the OpenQuake Engine input data, for seismic hazard calculations, are reported in supporting information S13.

- Bazzurro, P., & Cornell, C. A. (1999). Disaggregation of seismic hazard. *Bulletin of the Seismological Society of America*, 89, 501–520.
- Bertero, V., Mahin, S., & Herrera, R. (1978). Aseismic design implications of near-fault San Fernando earthquake records. *Earthquake Engineering & Structural Dynamics*, 6(1), 31–42. <https://doi.org/10.1002/eqe.4290060105>
- Bindi, D., Massa, M., Luzi, L., Ameri, G., Pacor, F., Puglia, R., & Augliera, P. (2014). Pan-European ground-motion prediction equations for the average horizontal component of PGA, PGV, and 5%-damped PSA at spectral periods up to 3.0 s using the RESORCE dataset (Vol. 12, p. 391, 2014). *Bulletin of Earthquake Engineering*, 12, 431–448.
- Bindi, D., Pacor, F., Luzi, L., Puglia, R., Massa, M., Ameri, G., & Paolucci, R. (2011). Ground motion prediction equations derived from the Italian strong motion database. *Bulletin of Earthquake Engineering*, 9(6), 1899–1920. <https://doi.org/10.1007/s10518-011-9313-z>
- Blumetti, A. M., Dramis, F., & Michetti, A. M. (1993). Fault-generated mountain fronts in the central Apennines (central Italy): Geomorphological features and seismotectonic implications. *Earth Surface Processes and Landforms*, 18(3), 203–223. <https://doi.org/10.1002/esp.3290180304>
- Bommer, J. J., & Abrahamson, N. A. (2006). Why Do Modern Probabilistic Seismic-Hazard Analyses Often Lead to Increased Hazard Estimates? *Bulletin of the Seismological Society of America*, 96, 1967–1977. <https://doi.org/10.1785/0120060043>
- Bommer, J. J., & Acevedo, A. B. (2004). The use of real earthquake accelerograms as input to dynamic analysis. *Journal of Earthquake Engineering*, 8(1), 43–91. <https://doi.org/10.1080/13632460409350521>
- Boncio, P., Lavecchia, G., Milana, G., & Rozzi, B. (2004a). Seismogenesis in central Apennines, Italy: An integrated analysis of minor earthquake sequences and structural data in the Amatrice-Campotosto area. *Annals of Geophysics*, 47(6), 1723–1742. <https://doi.org/10.4401/ag-7227>
- Boncio, P., Lavecchia, G., & Pace, B. (2004b). Defining a model of 3D seismogenic sources for seismic hazard assessment applications: The case of central Apennines (Italy). *Journal of Seismology*, 8(3), 407–425. <https://doi.org/10.1023/B:JOSE.0000038449.78801.05>
- Brozzetti, F., Boncio, P., Cirillo, D., Ferrarini, F., de Nardis, R., Testa, A., et al. (2019). High resolution field mapping and analysis of the August–October 2016 coseismic surface faulting (Central Italy Earthquakes): slip distribution, parameterization and comparison with global earthquakes. *Tectonics*, 38. <https://doi.org/10.1029/2018TC005305>
- Brozzetti, F., Boncio, P., Lavecchia, G., & Pace, B. (2009). Present activity and seismogenic potential of a low-angle normal fault system (Città di Castello, Italy): Constraints from surface geology, seismic reflection data and seismicity. *Tectonophysics*, 463(1–4), 31–46. <https://doi.org/10.1016/j.tecto.2008.09.023>
- Calamita, F., & Pizzi, A. (1992). Tettonica quaternaria nella dorsale appenninica umbro-marchigiana e bacini intrappenninici associati. *Studi Geologici Camerti*, 1992(1), 17–25.
- Carafa, M. M. C., & Bird, P. (2016). Improving deformation models by discounting transient signals in geodetic data: 2. Geodetic data, stress directions, and long-term strain rates in Italy. *Journal of Geophysical Research: Solid Earth*, 121, 5557–5575. <https://doi.org/10.1002/2016JB013038>
- Carlton, B., & Abrahamson, N. (2014). Issues and approaches for implementing conditional mean spectra in practice. *Bulletin of the Seismological Society of America*, 104(1), 503–512. <https://doi.org/10.1785/0120130129>
- Cauzzi, C., Faccioli, E., Vanini, M., & Bianchini, A. (2015). Updated predictive equations for broad-band (0.01–10 s) horizontal response spectra and peak ground motions, based on a global dataset of digital acceleration records. *Bulletin of Earthquake Engineering*, 13(6), 1587–1612. <https://doi.org/10.1007/s10518-014-9685-y>
- CEN (2004). Eurocode 8: “Design of structures for earthquake resistance—Part I: General rules, seismic actions and rules for buildings”, (EN-1998-1). Brussels, May 2004.
- Cheloni, D., De Novellis, V., Albano, M., Antonioli, A., Anzidei, M., Atzori, S., et al. (2017). Geodetic model of the 2016 central Italy earthquake sequence inferred from InSAR and GPS data. *Geophysical Research Letters*, 44, 6778–6787. <https://doi.org/10.1002/2017GL073580>
- Chiaraluce, L., Amato, A., Cocco, M., Chiarabba, C., Selvaggi, G., Di Bona, M., et al. (2004). Complex normal faulting in the Apennines thrust-and-fold belt: The 1997 seismic sequence in central Italy. *Bulletin of the Seismological Society of America*, 94(1), 99–116. <https://doi.org/10.1785/0120020052>
- Chiaraluce, L., Di Stefano, R., Tinti, E., Scognamiglio, L., Michele, M., Casarotti, E., et al. (2017). The 2016 central Italy seismic sequence: A first look at the mainshocks, aftershocks, and source models. *Seismological Research Letters*, 88(3), 757–771. <https://doi.org/10.1785/0220160221>
- Chiaraluce, L., Valoroso, L., Piccinini, D., Di Stefano, R., & De Gori, P. (2011). The anatomy of the 2009 L’Aquila normal fault system (central Italy) imaged by high resolution foreshock and aftershock locations. *Journal of Geophysical Research*, 116, B12311. <https://doi.org/10.1029/2011JB008352>
- Chioccarelli, E., & Iervolino, I. (2010). Near-source seismic demand and pulse-like records: A discussion for L’Aquila earthquake. *Earthquake Engineering & Structural Dynamics*, 39(9), 1039–1062.
- Chioccarelli, E., & Iervolino, I. (2014). Sensitivity analysis of directivity effects on PSHA. *Bollettino di Geofisica Teorica ed Applicata*, 55(1), 41–53. <https://doi.org/10.4430/bgta0099>
- Cinti, F. R., Pantosti, D., De Martini, P. M., Pucci, S., Civico, R., Pierdominici, S., et al. (2011). Evidence for surface faulting events along the Paganica fault prior to the 6 April 2009 L’Aquila earthquake (central Italy). *Journal of Geophysical Research*, 116, B07308. <https://doi.org/10.1029/2010JB007988>
- Civico, R., Pucci, S., Villani, F., Pizzimenti, L., De Martini, P. M., Nappi, R., & the Open EMERGEO Working Group (2018). Surface ruptures following the 30 October 2016 M_w 6.5 Norcia earthquake, central Italy. *Journal of Maps*, 14(2), 151–160. <https://doi.org/10.1080/17445647.2018.1441756>
- Cornell, C. A. (1968). Engineering seismic risk analysis. *Bulletin of the Seismological Society of America*, 58(5), 1583–1606.
- D’Addezio, G., Masana, E., & Pantosti, D. (2001). The holocene paleoseismicity of the Aremogna-cinque Miglia fault (central Italy). *Journal of Seismology*, 5(2), 181–205. <https://doi.org/10.1023/A:1011403408568>
- D’Agostino, N. (2014). Complete seismic release of tectonic strain and earthquake recurrence in the Apennines (Italy). *Geophysical Research Letters*, 41, 1155–1162. <https://doi.org/10.1002/2014GL059230>
- D’Agostino, N., Mantenuto, S., D’Anastasio, E., Avallone, A., Barchi, M., Collettini, C., et al. (2009). Contemporary crustal extension in the Umbria-Marche Apennines from regional CGPS networks and comparison between geodetic and seismic deformation. *Tectonophysics*, 476(1–2), 3–12. <https://doi.org/10.1016/j.tecto.2008.09.033>
- De Nardis, R., Garbin, M., Lavecchia, G., Pace, B., Peruzza, L., Priolo, E., et al. (2011). A temporary seismic monitoring of the Sulmona area (Abruzzo, Italy) for seismotectonic purposes. *Bollettino di Geofisica Teorica ed Applicata*, 52(4), 651–666. <https://doi.org/10.4430/bgta0026>
- Devoti, R., Esposito, A., Pietrantonio, G., Pisani, A. R., & Riguzzi, F. (2011). Evidence of large scale deformation patterns from GPS data in the Italian subduction boundary. *Earth and Planetary Science Letters*, 311(3–4), 230–241. <https://doi.org/10.1016/j.epsl.2011.09.034>

- European Standard EN 1998-1 (2004). *Eurocode 8: Design of structures for earthquake resistance, Part 1: General rules, seismic actions and rules for buildings*. Brussels, Belgium: Comité Européen de Normalisation.
- Falucci, E., Gori, S., Moro, M., Pisani, A. R., Melini, D., Galadini, F., & Fredi, P. (2011). The 2009 L'Aquila earthquake (Italy): What's next in the region? Hints from stress diffusion analysis and normal fault activity. *Earth and Planetary Science Letters*, *305*(3–4), 350–358. <https://doi.org/10.1016/j.epsl.2011.03.016>
- Field, E. H., Biasi, G. P., Bird, P., Dawson, T. E., Felzer, K. R., Jackson, D. D., Johnson, K. M., et al. (2015). Long-term time-dependent probabilities for the third uniform California earthquake rupture forecast (UCERF3). *Bulletin of the Seismological Society of America*, *105*(2A), 511–543. <https://doi.org/10.1785/0120140093>
- Field, E. H., Jackson, D. D., & Dolan, J. F. (1999). A mutually consistent seismic-hazard source model for Southern California. *Bulletin of the Seismological Society of America*, *89*(3), 559–578.
- Field, E. H., & Jordan, T. H. (2015). Time-dependent renewal-model probabilities when date of last earthquake is unknown. *Bulletin of Seismological Society of America*, *105*(1), 459–463. <https://doi.org/10.1785/0120140096>
- Frankel, A. (1995). Simulating strong motions of large earthquakes using recordings of small earthquakes: The Loma Prieta mainshock as a test case. *Bulletin of the Seismological Society of America*, *85*(4), 1144–1160. Retrieved from <http://www.bssaonline.org/content/85/4/1144.short>
- Galadini, F., & Galli, P. (2000). Active tectonics in the central Apennines (Italy)—input data for seismic hazard assessment. *Natural Hazards*, *22*(3), 225–268. Retrieved from <http://link.springer.com/article/10.1023/A:1008149531980>
- Galadini, F., & Galli, P. (2003). Paleoseismology of silent faults in the central Apennines (Italy): The Mt. Vettore and Laga Mts. faults. *Annals of Geophysics*, *46*(5), 815–836. <https://doi.org/10.4401/ag-3457>
- Galli, P., Castenetto, S., & Peronace, E. (2017). The macroseismic intensity distribution of the 30 October 2016 earthquake in central Italy (M_w 6.6): Seismotectonic implications. *Tectonics*, *36*, 2179–2191. <https://doi.org/10.1002/2017TC004583>
- Galli, P., Galadini, F., & Pantosti, D. (2008). Twenty years of paleoseismology in Italy. *Earth-Science Reviews*, *88*(1–2), 89–117. <https://doi.org/10.1016/j.earscirev.2008.01.001>
- Galli, P., Galderisi, A., Peronace, E., Giaccio, B., Hajadas, I., Messina, P., & Polpetta, F. (2017). Quante volte figliola? Confessioni sibylline di una giovane faglia. *NGTGS*, *36*, 41–45.
- Galli, P., Giaccio, B., & Messina, P. (2010). The 2009 central Italy earthquake seen through 0.5 Myr-long tectonic history of the L'Aquila faults system. *Quaternary Science Reviews*, *29*(27–28), 3768–3789. <https://doi.org/10.1016/j.quascirev.2010.08.018>
- Galli, P., Giaccio, B., Messina, P., Peronace, E., & Zuppi, G. M. (2011). Palaeoseismology of the L'Aquila faults (central Italy, 2009, M_w 6.3 earthquake): Implications for active fault linkage. *Geophysical Journal International*, *187*(3), 1119–1134. <https://doi.org/10.1111/j.1365-246X.2011.05233.x>
- Galli, P., Giaccio, B., Peronace, E., & Messina, P. (2015). Holocene paleoearthquakes and Early-Late Pleistocene slip rate on the Sulmona fault (central Apennines, Italy). *Bulletin of the Seismological Society of America*, *105*(1), 1–13. <https://doi.org/10.1785/0120140029>
- Galli, P., Messina, P., Giaccio, B., Peronace, E., & Quadrio, B. (2012). Early Pleistocene to Late Holocene activity of the Magnola fault (Fucino fault system, central Italy). *Bollettino di Geofisica Teorica ed Applicata*, *53*(4), 435–458. <https://doi.org/10.4430/bgt0054>
- García-Mayordomo, J., Gaspar-Escribano, J. M., & Benito, B. (2007). Seismic hazard assessment of the Province of Murcia (SE Spain): Analysis of source contribution to hazard. *Journal of Seismology*, *11*(4), 453–471. <https://doi.org/10.1007/s10950-007-9064-0>
- Gardner, J. K., & Knopoff, L. (1974). Is the sequence of earthquakes in Southern California, with aftershocks removed, Poissonian? *Bulletin of the Seismological Society of America*, *64*, 1363–1367.
- Gneiting, T., & Raftery, A. E. (2007). Strictly proper scoring rules, prediction, and estimation. *Journal of the American Statistical Association*, *102*(477), 359–378. <https://doi.org/10.1198/016214506000001437>
- Hanks, T. C., & Kanamori, H. (1979). A moment magnitude scale. *Journal of Geophysical Research*, *84*, 2348–2350. <https://doi.org/10.1029/JB084iB05p02348>
- Harris, R. A. (2003). “The mechanics of earthquakes and faulting - second edition” by Christopher H. Scholz. *Seismological Research Letters*, *74*(3), 333–333. <https://doi.org/10.1785/gssrl.74.3.333>
- Haselton, C. B., Baker, J. W., Bozorgnia, Y., Goulet, C. A., Kalkan, E., Luco, N., et al. (2009). Evaluation of ground motion selection and modification methods: Predicting median interstory drift response of buildings. PEER Report 2009–01, Pacific Earthquake Engineering Research Center, University of California, Berkeley.
- Helmstetter, A., Kagan, Y. Y., & Jackson, D. D. (2007). High-resolution time-independent grid-based forecast for $M \geq 5$ earthquakes in California. *Seismological Research Letters*, *78*(1), 78–86. <https://doi.org/10.1785/gssrl.78.1.78>
- International Association of Seismology and Physics of the Earth's Interior (2005). Summary of Magnitude Working Group recommendations on standard procedures for determining earthquake magnitudes from digital data, available at: ftp://ftp.iaspei.org/pub/commissions/CSOI/summary_of_WG_recommendations_2005.pdf (last access: December 2015).
- Iervolino, I., Baltzopoulos, G., Chioccarelli, E., & Suzuki, A. (2017). Seismic actions on structures in the near-source region of the 2016 central Italy sequence. *Bulletin of Earthquake Engineering*, *15*, 1–19. <https://doi.org/10.1007/s10518-017-0295-3>
- Iervolino, I., Chioccarelli, E., & Baltzopoulos, G. (2012). Inelastic displacement ratio of near-source pulse-like ground motions. *Earthquake Engineering and Structural Dynamics*, *41*, 2351–2357.
- Kagan, Y. Y. (2002). Seismic moment distribution revisited: I. Statistical results. *Geophysical Journal International*, *148*(3), 520–541. <https://doi.org/10.1046/j.1365-246x.2002.01594.x>
- Kagan, Y. Y., & Knopoff, L. (1977). Earthquake risk prediction as a stochastic process. *Physics of the Earth and Planetary Interiors*, *14*(2), 97–108. [https://doi.org/10.1016/0031-9201\(77\)90147-9](https://doi.org/10.1016/0031-9201(77)90147-9)
- Kamer, Y., & Hiemer, S. (2015). Data-driven spatial b value estimation with applications to California seismicity: To b or not to b. *Journal of Geophysical Research: Solid Earth*, *120*, 5191–5214. <https://doi.org/10.1002/2014JB011510>
- Lanzano, G., Luzi, L., Rotondi, R., Varini, E., & Marzocchi, W. (2017). Selection and ranking of the ground motion prediction equations for the new Italian hazard map (MPS16). *NGTGS*, *36*, 282–285.
- Lavecchia, G., Castaldo, R., de Nardis, R., De Novellis, V., Ferrarini, F., Pepe, S., et al. (2016). Ground deformation and source geometry of the 24 August 2016 Amatrice earthquake (Central Italy) investigated through analytical and numerical modeling of DInSAR measurements and structural-geological data. *Geophysical Research Letters*, *43*, 12,389–12,398. <https://doi.org/10.1002/2016GL071723>
- Lavecchia, G., Ferrarini, F., Brozzetti, F., De Nardis, R., Boncio, P., & Chiaraluca, L. (2012). From surface geology to aftershock analysis: Constraints on the geometry of the L'Aquila 2009 seismogenic fault system. *Italian Journal of Geosciences*, *131*(3), 330–347. <https://doi.org/10.3301/IJG.2012.24>
- Lin, T., Harmsen, S., Baker, J., & Luco, N. (2013). Conditional spectrum computation incorporating multiple causal earthquakes and ground motion prediction models. *Bulletin of the Seismological Society of America*, *103*(2a), 1103–1116. <https://doi.org/10.1785/0120110293>

- Matthews, M. V., Ellsworth, W. L., & Reasenberg, P. A. (2002). A Brownian model for recurrent earthquakes. *Bulletin of the Seismological Society of America*, 92(6), 2233–2250. <https://doi.org/10.1785/0120010267>
- Meletti, C., Marzocchi, W., Albarello, D., D'Amico, V., Luzi, L., & the MPS16 Working Group (2017). The new Italian seismic hazard model. *8th International INQUA Meeting on Paleoseismology, Active Tectonics and Archeoseismology (PATA), 13–16 November, 2017, New Zealand*, pp. 270–275.
- Meletti, C., Visini, F., D'Amico, V., & Rovida, A. (2016). Seismic hazard in central Italy and the 2016 Amatrice earthquake. *Annals of Geophysics*, 59, 1–8. <https://doi.org/10.4401/AG-7248>
- Moro, M., Gori, S., Falcucci, E., Saroli, M., Galadini, F., & Salvi, S. (2013). Historical earthquakes and variable kinematic behaviour of the 2009 L'Aquila seismic event (central Italy) causative fault, revealed by paleoseismological investigations. *Tectonophysics*, 583, 131–144. <https://doi.org/10.1016/j.tecto.2012.10.036>
- Norme Tecniche per le Costruzioni (2018). Decreto Ministeriale 17 gennaio 2018: Aggiornamento delle “Norme Tecniche per le Costruzioni”, Ministero delle Infrastrutture. GU Serie Generale n. 42 del 20-02-2018.
- Ordaz, M., & Reyes, C. (1999). Earthquake hazard in Mexico City: Observations versus computations. *Bulletin of the Seismological Society of America*, 89(5), 1379–1383.
- Pace, B., Albarello, D., Boncio, P., Dolce, M., Galli, P., Messina, P., Peruzza, L., et al. (2011). Predicted ground motion after the L'Aquila 2009 earthquake (Italy, M_w 6.3): Input spectra for seismic microzoning. *Bulletin of Earthquake Engineering*, 9, 199–230.
- Pace, B., Bocchini, G. M., & Boncio, P. (2014). Do static stress changes of a moderate-magnitude earthquake significantly modify the regional seismic hazard? Hints from the L'Aquila 2009 normal-faulting earthquake (M_w 6.3, central Italy). *Terra Nova*, 26(6), 430–439. <https://doi.org/10.1111/ter.12117>
- Pace, B., Boncio, P., Brozzetti, F., Lavecchia, G., & Visini, F. (2008). From regional seismic hazard to “scenario earthquakes” for seismic microzoning: A new methodological tool for the Celano project. *Soil Dynamics and Earthquake Engineering*, 28(10–11), 866–874. <https://doi.org/10.1016/j.soildyn.2007.11.001>
- Pace, B., Peruzza, L., Lavecchia, G., & Boncio, P. (2006). Layered seismogenic source model and probabilistic seismic-hazard analyses in central Italy. *Bulletin of the Seismological Society of America*, 96(1), 107–132. <https://doi.org/10.1785/0120040231>
- Pace, B., Visini, F., & Peruzza, L. (2016). FiSH: MATLAB tools to turn fault data into seismic-hazard models. *Seismological Research Letters*, 87(2A), 374–386. <https://doi.org/10.1785/0220150189>
- Pagani, M., Monelli, D., Weatherill, G., Danciu, L., Crow-ley, H., Silva, V., et al. (2014). OpenQuake engine: An open hazard (and risk) software for the global earthquake model. *Seismological Research Letters*, 85(3), 692–702. <https://doi.org/10.1785/0220130087>
- Pagliaroli, A. (2018). Key issues in seismic microzonation studies: Lessons from recent experiences in Italy. *Rivista Italiana di Geotecnica*, 1(1), 5–48. <https://doi.org/10.19199/2017.4.0557.1405.047>
- Pagliaroli, A., & Lanzo, G. (2008). Selection of real accelerograms for the seismic response analysis of the historical town of Nicastro (southern Italy) during the March 1638 Calabria earthquake. *Engineering Structures*, 30(8), 2211–2222. <https://doi.org/10.1016/j.engstruct.2007.06.002>
- Peruse, E., Benedetti, L., Fleury, J., Rizza, M., Puliti, I., Billant, J., et al. (2018). Coseismic slip vectors of 24 August and 30 October 2016 earthquakes in Central Italy: Oblique slip and regional kinematic implications. *Tectonics*, 37, 3760–3781. <https://doi.org/10.1029/2018TC005083>
- Peruzza, L., & Pace, B. (2002). Sensitivity analysis for seismic source characteristics to probabilistic seismic hazard assessment in central Apennines (Abruzzo area). *Bollettino di Geofisica Teorica ed Applicata*, 43(1–2), 79–100.
- Peruzza, L., Pace, B., & Cavallini, F. (2010). Error propagation in time-dependent probability of occurrence for characteristic earthquakes in Italy. *Journal of Seismology*, 14(1), 119–141. <https://doi.org/10.1007/s10950-008-9131-1>
- Peruzza, L., Pace, B., & Visini, F. (2011). Fault-based earthquake rupture forecast in central Italy: Remarks after the L'Aquila M_w 6.3 event. *Bulletin of the Seismological Society of America*, 101(1), 404–412. <https://doi.org/10.1785/0120090276>
- Pucci, S., De Martini, P. M., Civico, R., Villani, F., Nappi, R., Ricci, T., et al. (2017). Coseismic ruptures of the 24 August 2016, M_w 6.0 Amatrice earthquake (central Italy). *Geophysical Research Letters*, 44, 2138–2147. <https://doi.org/10.1002/2016GL071859>
- Roberts, G. P., & Michetti, A. M. (2004). Spatial and temporal variations in growth rates along active normal fault systems: An example from the Lazio-Abruzzo Apennines, central Italy. *Journal of Structural Geology*, 26(2), 339–376. [https://doi.org/10.1016/S0191-8141\(03\)00103-2](https://doi.org/10.1016/S0191-8141(03)00103-2)
- Rovida, A., Locati, M., Camassi, R., Lolli, B., & Gasperini, P. (2016). CPTI15, the 2015 version of the parametric catalogue of Italian earthquakes. *Istituto Nazionale di Geofisica e Vulcanologia*. <https://doi.org/10.6092/INGV.IT-CPTI15>
- Salvi, S., Cinti, F. R., Colini, L., D'Addezio, G., Doumaz, F., & Pettinelli, E. (2003). Investigation of the active Celano-L'Aquila fault system, Abruzzi (central Apennines, Italy) with combined ground-penetrating radar and palaeoseismic trenching. *Geophysical Journal International*, 155(3), 805–818. <https://doi.org/10.1111/j.1365-246X.2003.02078.x>
- Scherbaum, F., Delavaud, E., & Riggelsen, C. (2009). Model selection in seismic hazard analysis: An information—Theoretic perspective. *Bulletin of the Seismological Society of America*, 99(6), 3234–3247. <https://doi.org/10.1785/0120080347>
- Schlagenhauf, A., Manighetti, I., Benedetti, L., Gaudemer, Y., Finkel, R., Malavieille, J., & Pou, K. (2011). Earthquake supercycles in central Italy, inferred from ^{36}Cl exposure dating. *Earth and Planetary Science Letters*, 307(3–4), 487–500. <https://doi.org/10.1016/j.epsl.2011.05.022>
- Scholz, C. H. (1988). The brittle-plastic transition and the depth of seismic faulting. *Geologische Rundschau*, 77(1), 319–328. <https://doi.org/10.1007/BF01848693>
- Scotti, O., Clément, C., & Baumont, D. (2014). Seismic hazard for design and verification of nuclear installations in France: Regulatory context, debated issues and ongoing developments. *Bollettino di Geofisica Teorica ed Applicata*, 55, 135–148. <https://doi.org/10.4430/bgta0080>
- Sibson, R. H. (1983). Continental fault structure and the shallow earthquake source. *Journal of the Geological Society*, 140(5), 741–767. <https://doi.org/10.1144/gsjgs.140.5.0741>
- Sibson, R. H. (1989). Earthquake faulting as a structural process. *Journal of Structural Geology*, 11(1–2), 1–14. [https://doi.org/10.1016/0191-8141\(89\)90032-1](https://doi.org/10.1016/0191-8141(89)90032-1)
- Sibson, R. H. (2003). Thickness of the seismic slip zone. *Bulletin of the Seismological Society of America*, 93(3), 1169–1178. <https://doi.org/10.1785/0120020061>
- SM Working Group (2015). Guidelines for seismic microzonation. *Civil Protection Department and Conference of Regions and Autonomous Provinces of Italy. 1 Vol.* English edition of: Gruppo di lavoro MS, Indirizzi e criteri per la microzonazione sismica, Conferenza delle Regioni e delle Province autonome – Dipartimento della protezione civile, Roma, 2008, 3 vol. e Dvd. Available online at http://www.protezionecivile.gov.it/httpdocs/cms/attach_extra/GuidelinesForSeismicMicrozonation.pdf
- Stucchi, M., Meletti, C., Montaldo, V., Crowley, H., Calvi, G. M., & Boschi, E. (2011). Seismic hazard assessment (2003–2009) for the Italian building code. *Bulletin of the Seismological Society of America*, 101(4), 1885–1911. <https://doi.org/10.1785/0120100130>

- TC4-ISSMGE (1993; Revised 1999). Manual for zonation on seismic geotechnical hazards. *Technical Committee for Earthquake Geotechnical Engineering*.
- Valentini, A., Visini, F., & Pace, B. (2017). Integrating faults and past earthquakes into a probabilistic seismic hazard model for peninsular Italy. *Natural Hazards and Earth System Sciences*, 17(11), 2017–2039. <https://doi.org/10.5194/nhess-17-2017-2017>
- Valoroso, L., Chiaraluce, L., Piccinini, D., Di Stefano, R., Schaff, D., & Waldhauser, F. (2013). Radiography of a normal fault system by 64,000 high-precision earthquake locations: The 2009 L'Aquila (central Italy) case study. *Journal of Geophysical Research: Solid Earth*, 118, 1156–1176. <https://doi.org/10.1002/jgrb.50130>
- Verdecchia, A., Pace, B., Visini, F., Scotti, O., Peruzza, L., & Benedetti, L. (2018). The role of viscoelastic stress transfer in long-term earthquake cascades: Insights after the central Italy 2016–2017 seismic sequence. *Tectonics*, 37, 3411–3428. <https://doi.org/10.1029/2018TC005110>
- Villani, F., Civico, R., Pucci, S., Pizzimenti, L., Nappi, R., De Martini, P. M., & the Open EMERGEIO Working Group (2018). A database of the coseismic effects following the 30 October 2016 Norcia earthquake in central Italy. *Scientific Data*, 5, 180049. <https://doi.org/10.1038/sdata.2018.49>
- Visini, F., & Pace, B. (2014). Insights on a key parameter of earthquake forecasting, the coefficient of variation of the recurrence time, using a simple earthquake simulator. *Seismological Research Letters*, 85(3), 703–713. <https://doi.org/10.1785/0220130165>
- Wells, D. L., & Coppersmith, K. J. (1994). New empirical relationships among magnitude, rupture length, rupture width, rupture area, and surface displacement. *Bulletin of the Seismological Society of America*, 84(4), 974–1002.
- Woessner, J., Laurentiu, D., Giardini, D., Crowley, H., Cotton, F., Grünthal, G., et al. (2015). The 2013 European seismic hazard model: Key components and results. *Bulletin of Earthquake Engineering*, 13(12), 3553–3596. <https://doi.org/10.1007/s10518-015-9795-1>
- Zechar, J. D., & Zhuang, J. (2014). A parimutuel gambling perspective to compare probabilistic seismicity forecasts. *Geophysical Journal International*, 199(1), 60–68. <https://doi.org/10.1093/gji/ggu137>